Calculation of Laminar Heating Rates on Three-Dimensional Configurations Using the Axisymmetric Analogue

H. Harris Hamilton II

NASA

NASA Technical Paper 1698

Calculation of Laminar Heating Rates on Three-Dimensional Configurations Using the Axisymmetric Analogue

H. Harris Hamilton II
Langley Research Center
Hampton, Virginia

SUMMARY

A theoretical method has been developed for computing approximate laminar
heating rates on three-dimensional configurations at angle of attack. The
method is based on the axisymmetric analogue which is used to reduce the three-
dimensional boundary-layer equations along surface streamlines to an equivalent
axisymmetric form by using the metric coefficient which describes streamline
divergence (or convergence). The method has been coupled with a three-
dimensional inviscid flow field program for computing surface streamline paths,
metric coefficients, and boundary-layer edge conditions. Good agreement has
been obtained with experimental data on a spherically blunted 15° half-angle
cone, a spherically blunted 80° sweep slab delta wing, and a Space Shuttle
Orbiter type configuration at angles of attack up to 25°. The method provides
a useful means of computing heating rates on advanced entry configurations.

INTRODUCTION

With the development of the Space Shuttle transportation system well under
way, attention is being focused on more advanced Earth orbital transportation
systems which will be expected to replace the Space Shuttle system near the end
of this century. These vehicles will be subjected to severe aerodynamic heating
during reentry, and the design of their thermal protection systems will require
detailed information on surface heating rates. Three-dimensional winged config-
urations are currently being considered (refs. 1 and 2) and they will probably
fly at relatively large angles of attack. It will first be necessary to compute
the three-dimensional viscous flow over the vehicle in order to accurately pre-
dict the surface heating rates.

With advances in high-speed computers and numerical techniques, much prog-
ress has been made in recent years in computing viscous compressible flows using
the Navier-Stokes equations (ref. 3). However, solutions for general three-
dimensional winged configurations are far beyond the "state of the art" of cur-
rent applications, and their demand on computer resources would far exceed the
capabilities of the current generation of computers.

Much of the needed information on surface heating rates can be obtained
from a "classical approach" where the outer inviscid flow field is computed
independent of the boundary layer and is used to provide edge conditions for a
three-dimensional boundary-layer calculation near the surface. Solutions have
been obtained for the general three-dimensional compressible boundary-layer
equations. (See, for example, refs. 4 to 8.) To date, the application of these
methods has been limited to relatively simple geometries. An attempt has been
made to extend the method of reference 5 to more realistic configurations; but,
it has not yet been successful. However, even if these methods could be applied
to the configurations of interest in the present study, their use would be cost
prohibitive for design calculations.

Cooke has developed an axisymmetric analogue for the general three-dimensional compressible boundary-layer equations (ref. 9) which greatly simplifies the calculation of three-dimensional viscous flows. Following that approach, the general three-dimensional boundary-layer equations are written in streamline coordinates and the cross-flow velocities (tangent to the surface and normal to streamline direction) are assumed zero. This reduces the three-dimensional boundary-layer equations to a form identical to that for axisymmetric flow provided: (1) the distance along a streamline is interpreted as distance along an "equivalent axisymmetric body" and (2) the metric that describes the spreading of the streamlines is interpreted as the radius of the equivalent axisymmetric body. This allows any existing axisymmetric boundary-layer program to be used to compute three-dimensional heating rates along a streamline in regions where the small cross-flow assumption is valid. By considering multiple streamline paths, an entire vehicle can be covered.

Hayes (ref. 10) has shown that the cross flow in the boundary layer is small when the streamline curvature is small. Vaglio-Laurin (ref. 11) has shown that when the wall is highly cooled the cross flow in the boundary layer is small even for cases where the streamline curvature is not small. Further, in references 12 to 14, for example, comparisons with experimental data and other theoretical calculations, including some cases where the cross flow in the boundary layer is not small, indicate that reasonably accurate heating rates can be obtained using the axisymmetric analogue.

The most obvious difficulty in applying this technique is that of computing the three-dimensional inviscid flow field from which the surface streamline pattern and the metrics are determined. In reference 15, DeJarnette and Hamilton present a relatively simple method of calculating the streamline location and metric coefficient along the streamline from a known surface pressure distribution. With this approach the path of a single streamline is computed on the surface; simultaneously, a second-order differential equation is solved along the streamline for the metric. The major difficulty with this approach is that second derivatives of the surface pressure are required to calculate the metric. These are very difficult to obtain with sufficient accuracy from either experimental measurements or approximate methods (such as Newtonian theory) except for a few simple cases. In reference 16, DeJarnette presents an improved method for calculating the inviscid surface streamlines. Two adjacent streamlines are computed from a known surface pressure distribution, using only first derivatives of the pressure; and the metric is obtained by determining the rate at which the streamlines spread on the surface. This is a much better approach since it relaxes some requirements upon the accuracy of the input surface pressure distribution. However, it still requires more detailed pressure distributions than are generally available from most experimental studies.

In both references 17 and 18, methods have been presented for computing the metric coefficient on the surface of a body from an inviscid flow field solution. However, in each case it would be very difficult to accurately compute the metric coefficient at the boundary-layer edge using these methods. Although this will not be considered in the present paper, it is important that the chosen technique should not have such a limitation. Since in the present approach, the metric coefficient is computed from information on two adjacent streamlines,

it will be very easy to extend the method to use boundary-layer edge conditions to compute the metric coefficient at the boundary-layer edge.

Recently, a method has been developed for computing the three-dimensional inviscid flow field over general configurations at angle of attack. (See refs. 17 and 19.) Using information about the velocity directions from the inviscid solution, streamlines can be traced on the vehicle surface. Then, a method similar to that presented by DeJarnette (ref. 16) can be used to compute the metrics along each streamline. This approach offers the advantage of computing heating rates on three-dimensional vehicles without requiring experimental pressure distributions.

In the present paper, an axisymmetric analogue method for computing heating rates on three-dimensional configurations at angle of attack is developed. The necessary inviscid streamline information was obtained using the inviscid-solution procedure of reference 17. The accuracy of this solution technique is demonstrated by direct comparison of computed heating rates with experimental data.

The information presented in this report was included in a report entitled "Calculation of Heating Rates on Three-Dimensional Configurations" submitted in partial fulfillment of the requirements for the Degree of Engineer, The George Washington University, December 1979.

SYMBOLS

A	parameter in transformation from cylindrical to local polar coordinates
$\bar{A}$	parameter in transformation from local polar to cylindrical coordinates
c_p	specific heat at constant pressure, J/kg-K
c_v	specific heat at constant volume, J/kg-K
h	static enthalpy, J/kg
h_e	local enthalpy at edge of boundary layer, J/kg
h_r	reference heat-transfer coefficient, W/m^2-s-K
h_s	stagnation-point heat-transfer coefficient, W/m^2-s-K
h_w	heat-transfer coefficient at wall, W/m^2-s-K
h_1	metric coefficient in ξ-direction, m
h_2	metric coefficient in β-direction, m

H	total enthalpy, J/kg
k	thermal conductivity, W/m-K
$\bar{k}$	streamline curvature, 1/m
L	length, m
l	distance measured along leading edge of delta wing, m
M	Mach number
N_{Pr}	Prandtl number, $c_p\mu/k$
N_{Re}	unit Reynolds number
n	distance normal to surface, m
p	pressure, N/m^2
q	heat-transfer rate, W/m^2
q	distance normal to streamline on surface, m
RF	recovery factor
R_n	radius of curvature of spherical nose, m
r_0	displacement of coordinate pole, m
R,Φ,χ	local polar coordinates (see fig. 4)
r,ϕ,x	cylindrical coordinates (see fig. 4)
S	constant in Sutherland's viscosity law, K
s	distance along streamline, m
$\bar{s}$	arc length, m
T	temperature, K
t_e	ratio of enthalpies, h_e/H_e
u	velocity component in ξ-direction, m/s
V_∞	free-stream velocity, m/s
v	velocity component in β-direction, m/s
v_t	velocity component defined by equation (B1), m/s

4

$\bar{v}_n$ velocity component defined by equation (B2), m/s

w velocity component in n-direction, m/s

w_t velocity component defined by equation (B3), m/s

w_1, w_2, w_3 Cartesian velocity components defined by sketch (a) of appendix B, m/s

x, y, z Cartesian coordinates (see fig. 5)

α angle of attack

β coordinate normal to streamline on surface

$\bar{\beta}$ boundary-layer velocity gradient parameter

Γ geometry angle defined by equation (22) (see sketch (c) of appendix B)

γ ratio of specific heats, c_p/c_v

δ_ϕ geometry angle defined by equation (21) (see sketch (b) of appendix B)

ζ_w ratio of total enthalpies, H_w/H_e

ζ_w' slope of total enthalpy profile at wall, $\left[\dfrac{\partial (H/H_e)}{\partial \bar{\eta}}\right]_w$

$\bar{\eta}$ transformed boundary-layer coordinate normal to wall

θ angle defining velocity direction on surface measured relative to meridional plane (see fig. 8)

μ viscosity, $N\text{-}s/m^2$

ξ coordinate along streamline on surface

$\bar{\xi}$ transformed boundary-layer coordinate along surface streamline

ρ density, kg/m^3

$\bar{\Phi}$ dissipation function, W/m^3

Subscripts:

b   body

max   maximum

e   edge of boundary layer

s   inviscid stagnation point

w   wall

∞   free stream

METHOD OF SOLUTION

In the sections that follow, a method for calculating heating rates on three-dimensional configurations using the axisymmetric analogue (ref. 9) is described, and the equations necessary for applying the technique are developed. The assumptions made from the outset are that: (1) the Reynolds number of the flow is sufficiently large so that boundary-layer concepts apply; (2) the fluid is a perfect gas; (3) the flow is laminar; and (4) the entropy at the edge of the boundary layer is constant. Although the last three assumptions are not necessary, they will simplify the development of the technique.

Axisymmetric Analogue

Consider an orthogonal streamline coordinate system (ξ, β, n) where ξ is directed along an inviscid surface streamline and n is distance measured along the outward normal from the surface (fig. 1). The element of arc length $d\bar{s}$ in such a curvilinear coordinate system is given by the equation

$$d\bar{s}^2 = h_1^2 d\xi^2 + h_2^2 d\beta^2 + dn^2 \tag{1}$$

where h_1 and h_2 are metric coefficients. By restricting attention to a thin boundary-layer region near the surface, both h_1 and h_2 can be assumed to be functions of ξ and β only.

Taking the velocity components in the ξ-, β-, and n-directions as u, v, and w, respectively, the general three-dimensional boundary-layer equations can be written as follows (ref. 9):

Continuity

$$\frac{1}{h_1 h_2}\left[\frac{\partial}{\partial\xi}(\rho h_2 u) + \frac{\partial}{\partial\beta}(\rho h_1 v) + \frac{\partial}{\partial n}(\rho h_1 h_2 w)\right] = 0 \tag{2}$$

6

ξ-momentum

$$\rho\left(\frac{u}{h_1}\frac{\partial u}{\partial \xi} + \frac{v}{h_2}\frac{\partial u}{\partial \beta} + w\frac{\partial u}{\partial n} + \frac{uv}{h_1 h_2}\frac{\partial h_1}{\partial \beta} - \frac{v^2}{h_1 h_2}\frac{\partial h_2}{\partial \xi}\right)$$

$$= -\frac{1}{h_1}\frac{\partial p}{\partial \xi} + \frac{\partial}{\partial n}\left(\mu\frac{\partial u}{\partial n}\right) \tag{3}$$

β-momentum

$$\rho\left(\frac{u}{h_1}\frac{\partial v}{\partial \xi} + \frac{v}{h_2}\frac{\partial v}{\partial \beta} + w\frac{\partial v}{\partial n} + \frac{uv}{h_1 h_2}\frac{\partial h_2}{\partial \xi} - \frac{u^2}{h_1 h_2}\frac{\partial h_1}{\partial \beta}\right)$$

$$= -\frac{1}{h_2}\frac{\partial p}{\partial \beta} + \frac{\partial}{\partial n}\left(\mu\frac{\partial v}{\partial n}\right) \tag{4}$$

n-momentum

$$\frac{\partial p}{\partial n} = 0 \tag{5}$$

Energy

$$\rho c_p\left(\frac{u}{h_1}\frac{\partial T}{\partial \xi} + \frac{v}{h_2}\frac{\partial T}{\partial \beta} + w\frac{\partial T}{\partial n}\right) = \bar{\Phi} + \frac{u}{h_1}\frac{\partial p}{\partial \xi}$$

$$+ \frac{v}{h_2}\frac{\partial p}{\partial \beta} + w\frac{\partial p}{\partial n} + \frac{\partial}{\partial n}\left(k\frac{\partial T}{\partial n}\right) \tag{6}$$

where $\bar{\Phi}$ is the dissipation function. (See ref. 9.)

It is convenient to express derivatives in the ξ-direction in terms of the distance s along a streamline as

$$\frac{1}{h_1}\frac{\partial}{\partial \xi} = \frac{\partial}{\partial s}$$

Further, it is assumed that the cross-flow velocity v and its derivatives are small. With these simplifications, equations (2), (3), (5), (6), and (4) are as follows:

Continuity

$$\frac{\partial}{\partial s}(\rho h_2 u) + \frac{\partial}{\partial n}(\rho h_2 w) = 0 \tag{7}$$

s-momentum

$$\rho\left(u\frac{\partial u}{\partial s} + w\frac{\partial u}{\partial n}\right) = -\frac{\partial p}{\partial s} + \frac{\partial}{\partial n}\left(\mu\frac{\partial u}{\partial n}\right) \tag{8}$$

n-momentum

$$\frac{\partial p}{\partial n} = 0 \tag{9}$$

Energy

$$\rho c_p\left(u\frac{\partial T}{\partial s} + w\frac{\partial T}{\partial n}\right) = u\frac{\partial p}{\partial s} + \frac{\partial}{\partial n}\left(k\frac{\partial T}{\partial n}\right) + \mu\left(\frac{\partial u}{\partial n}\right)^2 \tag{10}$$

β-momentum

$$\rho\left(u\frac{\partial v}{\partial s} + w\frac{\partial v}{\partial n} + \frac{uv}{h_2}\frac{\partial h_2}{\partial s} - \bar{k}u^2\right) = -\frac{1}{h_2}\frac{\partial p}{\partial \beta} + \frac{\partial}{\partial n}\left(\mu\frac{\partial v}{\partial n}\right) \tag{11}$$

where $\bar{k}$ is the streamline curvature term given by the equation

$$\bar{k} = \frac{1}{h_1 h_2}\frac{\partial h_1}{\partial \beta} \tag{12}$$

8

Equations (7) to (10) are identical to the usual axisymmetric boundary-layer equations (ref. 20) if s is interpreted as distance along an "equivalent axisymmetric body" and h_2 is interpreted as the radius of that body. This set of equations can be solved for u, w, ρ, and T through the boundary layer along a streamline using one of the many methods that have been developed for solving the axisymmetric boundary-layer equations (for example, refs. 21 and 22). With u, w, ρ, and T assumed known from a previous solution, equation (11) becomes a linear equation which can easily be solved for v, the cross-flow velocity component. In the present application, only the heat transfer is of interest; thus it is unnecessary to solve the cross-flow momentum equation since in the axisymmetric analogue it has no effect on heating rates.

Coordinate System and Surface Geometry

The present paper is concerned with calculating heating rates on three-dimensional configurations – typical of the configuration illustrated in figure 2 – which are symmetric about the XZ-plane (pitch plane). The fuselage of these vehicles can be easily described in cylindrical coordinates (r_b, ϕ, x) using a function of the form (fig. 3)

$$r_b = r_b(\phi, x) \tag{13}$$

where the pole of the coordinate system is located on the X-axis. However, when wings extend from the fuselage, equation (13) may become multivalued. (See fig. 4.) One solution to this problem is to allow the pole to be a function of x

$$r_0 = r_0(x) \tag{14}$$

Then, at a given x-station, the pole can be located such that r_b is a single-valued function. This new coordinate system R_b, Φ, χ will be called a "local polar coordinate system" in which the vehicle surface can be represented by a function of the form

$$R_b = R_b(\Phi, \chi) \tag{15}$$

which is much more general than equation (13). It should be noted that the new coordinate system is generally nonorthogonal; however, for the special case where $r_0(x) = 0$, it reduces to the standard cylindrical coordinate system which is orthogonal.

Vachris and Yaeger (ref. 23) have developed a computer program called QUICK which uses the local polar coordinate system to describe vehicle geometries. In this program, analytic curves are patched together to give a functional repre-

sentation of the vehicle geometry similar in form to equation (15). The QUICK program is compatible with the method that will be used to obtain the inviscid flow field solution (refs. 17 and 19). Thus, it will be used exclusively in the present study to describe vehicle surface geometry.

The detailed relationship between local polar and cylindrical coordinates on a surface are given in appendix A, but the transformation equations are summarized here for convenience. First, the equations describing the transformation from cylindrical coordinates r_b, ϕ, x to local polar coordinates R_b, Φ, χ on a surface are

$$R_b = r_b \sqrt{A^2 + 1} \, \cos \phi \tag{16a}$$

$$\Phi = \tan^{-1} A \tag{16b}$$

$$\chi = x \tag{16c}$$

where

$$A = \tan \phi - r_0(x)/(r_b \cos \phi) \tag{16d}$$

Similarly, the inverse transformation from local polar coordinates R_b, Φ, χ to cylindrical coordinates on a surface is expressed as

$$r_b = R_b \sqrt{\bar{A}^2 + 1} \, \cos \Phi \tag{17a}$$

$$\phi = \tan^{-1} \bar{A} \tag{17b}$$

$$x = \chi \tag{17c}$$

where

$$\bar{A} = \tan \Phi + r_0(\chi)/(R_b \cos \Phi) \tag{17d}$$

Since the vehicle geometry will be obtained from the QUICK program in the functional form of equation (15), the inverse transformation equations should be more useful.

Calculation of Inviscid Surface Streamlines

and Metric Coefficients

One of the most difficult steps in applying the axisymmetric analogue is calculating the inviscid surface streamlines and the metric coefficient h_2 along each streamline. In the present study the inviscid streamline information will be calculated using the results of a set of three-dimensional inviscid flow field programs described in references 17, 19, and 24. The manner in which the flow field is calculated is illustrated in figure 5. First, the subsonic/transonic flow over the nose is computed using a time dependent method BLUNT similar to that described in reference 24. From this solution an initial data plane (IDP) normal to the χ-axis is obtained, in a region where the flow is entirely supersonic. Then, a finite-difference marching technique STEIN (refs. 17 and 19) is used to continue the solution downstream in the supersonic region step by step in planes normal to the χ-axis. These solutions provide the inviscid flow field data over the entire vehicle which will be used to calculate the streamlines and metric coefficients.

Nose region.- In the nose region of a blunt body, the surface streamlines originate at the stagnation point as illustrated in figure 6. Letting ξ be the coordinate in the streamline direction and β the coordinate in a direction normal to the streamline and tangent to the surface, the differentials of arc length are

$$ds = h_1 \, d\xi \tag{18a}$$

and

$$dq = h_2 \, d\beta \tag{18b}$$

respectively. The metric coefficient h_2 gives a measure of the divergence or convergence of the streamlines on the surface and is the "equivalent radius" that must be used in the axisymmetric boundary-layer equations.

The nose geometry of most nonablating blunt reentry vehicles is smooth; thus, the pressure distribution in the nose region of these vehicles is also relatively smooth. Because of this, the pressures can be computed by BLUNT and used as inputs to the computer program described in reference 16 to calculate the streamlines and metric coefficients from the stagnation point to the station where the initial data plane intersects the body surface. (See fig. 6.) In principle, the same technique could be used to continue the streamline solutions downstream; but it could lead to large inaccuracies since the pressure distribution can change radically downstream of the nose on general three-dimensional

configurations. Thus, downstream of the IDP, a new technique for obtaining streamline solutions has been developed, and it will be described in detail in the next section.

Downstream supersonic region.- DeJarnette (ref. 16) presents the following two equations which can be used to calculate the streamline position:

$$\left(\frac{\partial \phi}{\partial x}\right)_\beta = \frac{1}{r_b}\left(\frac{\tan \theta \cos \delta_\phi}{\cos \Gamma} - \tan \Gamma \sin \delta_\phi\right) \tag{19}$$

and the metric coefficient h_2

$$\left(\frac{\partial \phi}{\partial \beta}\right)_x = \left(\frac{\cos \delta_\phi}{r_b \cos \theta}\right)h_2 \tag{20}$$

The angles δ_ϕ and Γ are the body-geometry angles defined in reference 15. (See also fig. 7.) They are given by the equations

$$\tan \delta_\phi = \frac{1}{r_b}\left(\frac{\partial r_b}{\partial \phi}\right)_x \tag{21}$$

and

$$\tan \Gamma = \cos \delta_\phi \left(\frac{\partial r_b}{\partial x}\right)_\phi \tag{22}$$

The angle θ is related to the velocity direction on the surface (fig. 8) and can be obtained from the inviscid flow field solution.

The distance along a streamline can be calculated from the following differential equation:

$$\left(\frac{\partial s}{\partial x}\right)_\beta = \frac{1}{\cos \theta \cos \Gamma} \tag{23}$$

Since β is constant on a given streamline, equation (19) can be integrated along a streamline to determine the variation of the cylindrical angle ϕ with respect to x. Similarly, equation (23) can be integrated to give the streamline length. To obtain the metric coefficient along a streamline, the primary streamline – the streamline along which heating rates are calculated – and an adjacent streamline (separated from the primary streamline by $\Delta\beta$) are computed simultaneously. Then, at a given x-station the metric coefficient h_2 is computed from equation (20) after first approximating the derivative $(\partial\phi/\partial\beta)_x$ numerically using one-sided differences. In reference 16 numerical experiments were performed using several types of difference schemes to approximate $(\partial\phi/\partial\beta)_x$ and the preceding procedure was found to be sufficiently accurate.

The angles δ_ϕ and Γ given by equations (21) and (22) are defined in terms of cylindrical coordinates ϕ and x. In order to apply these equations to general wing-body configurations, they must be transformed to local polar coordinates. This transformation leads to the following results (see appendix A for details):

$$
\tan \delta_\phi = \frac{\left(\dfrac{\partial \Phi}{\partial \phi}\right)_x \left(\dfrac{\partial r_b}{\partial \Phi}\right)_\chi}{R_b \sqrt{1 + \bar{A}^2}\; \cos \Phi}
\tag{24}
$$

and

$$
\tan \Gamma = \cos \delta_\phi \left[\left(\frac{\partial \Phi}{\partial x}\right)_\phi \left(\frac{\partial r_b}{\partial \Phi}\right)_\chi + \left(\frac{\partial r_b}{\partial \chi}\right)_\Phi \right]
\tag{25}
$$

where

$$
\left(\frac{\partial \Phi}{\partial \phi}\right)_x = \frac{\left(1 + \bar{A}^2\right)\left(R_b^2 \cos^2 \Phi\right)}{R_b^2 + r_0 \left[R_b \sin \Phi - \left(\dfrac{\partial R_b}{\partial \Phi}\right)_\chi \cos \Phi \right]}
\tag{26}
$$

$$
\left(\frac{\partial \bar{A}}{\partial \Phi}\right)_\chi = \frac{1}{R_b^2 \cos^2 \Phi} \left\{ R_b^2 + r_0 \left[R_b \sin \Phi - \left(\frac{\partial R_b}{\partial \Phi}\right)_\chi \cos \Phi \right] \right\}
\tag{27}
$$

13

$$\left(\frac{\partial r_b}{\partial \Phi}\right)_\chi = R_b\sqrt{1 + \bar{A}^2} \ \cos \ \Phi\left[\frac{1}{R_b}\left(\frac{\partial R_b}{\partial \Phi}\right)_\chi + \frac{\bar{A}}{1 + \bar{A}^2}\left(\frac{\partial \bar{A}}{\partial \Phi}\right)_\chi - \tan \ \Phi\right] \tag{28}$$

$$\left(\frac{\partial r_b}{\partial \chi}\right)_\Phi = R_b\sqrt{1 + \bar{A}^2} \ \cos \ \Phi\left[\frac{1}{R_b}\left(\frac{\partial R_b}{\partial \chi}\right)_\Phi + \frac{\bar{A}}{1 + \bar{A}^2}\left(\frac{\partial \bar{A}}{\partial \chi}\right)_\Phi\right] \tag{29}$$

The derivatives $\left(\dfrac{\partial R_b}{\partial \Phi}\right)_\chi$ and $\left(\dfrac{\partial R_b}{\partial \chi}\right)_\Phi$ are obtained from the geometry description program QUICK.

Similarly, equation (19) gives the location of the streamline in terms of the cylindrical angle ϕ. For wing-body configurations, the angle ϕ may not describe a unique point on the body cross section. (See fig. 4.) To avoid this problem, equation (19) can be rewritten in terms of the local polar angle Φ in the following form (see appendix A for details):

$$\left(\frac{\partial \Phi}{\partial \chi}\right)_\beta = \left(1 + \bar{A}^2\right)\left(\frac{R_b \ \cos^2 \ \Phi}{R_b + r_0 \ \sin \ \Phi}\right)\left\{\left(\frac{\partial \phi}{\partial x}\right)_\beta + \frac{1}{R_b \ \cos \ \Phi}\left[\frac{r_0}{R_b}\left(\frac{\partial R_b}{\partial x}\right)_\beta - \frac{dr_0}{d\chi}\right]\right\} \tag{30}$$

where

$$\left(\frac{\partial R_b}{\partial x}\right)_\beta = \left[\left(\frac{\partial \Phi}{\partial x}\right)_\phi + \left(\frac{\partial \phi}{\partial x}\right)_\beta\left(\frac{\partial \Phi}{\partial \phi}\right)_x\right]\left(\frac{\partial R_b}{\partial \Phi}\right)_\chi + \left(\frac{\partial R_b}{\partial \chi}\right)_\Phi \tag{31}$$

$$\left(\frac{\partial \Phi}{\partial x}\right)_\phi = -R_b \ \cos \ \Phi\left\{\frac{\dfrac{dr_0}{d\chi} - \dfrac{r_0}{R_b}\left(\dfrac{\partial R_b}{\partial \chi}\right)_\phi}{R_b^2 + r_0\left[R_b \ \sin \ \Phi - \left(\dfrac{\partial R_b}{\partial \Phi}\right)_\chi \ \cos \ \Phi\right]}\right\} \tag{32}$$

14

and where $\left(\dfrac{\partial \phi}{\partial x}\right)_\beta$ and $\left(\dfrac{\partial \Phi}{\partial \phi}\right)_x$ are given by equations (19) and (26), respec-

tively, and $\left(\dfrac{\partial R_b}{\partial \Phi}\right)_\chi$, $\left(\dfrac{\partial R_b}{\partial \chi}\right)_\Phi$, and $\dfrac{dr_0}{d\chi}$ are calculated in the geometry descrip-
tion program QUICK.

After obtaining the angle θ, which is related to the velocity direction on the surface, from the inviscid solution (appendix B), equation (30) can be integrated to obtain the streamline location on the body surface as a function of Φ and χ. This is a general equation and can be applied to any configuration where the pole can be located to give R_b as a single-valued function of Φ and χ. (See fig. 4.) For the special case where $r_0 = 0$, the local polar coordinate system reduces to a cylindrical coordinate system, and equation (30) reduces to the form

$$\left(\frac{\partial \Phi}{\partial \chi}\right)_\beta = \left(\frac{\partial \phi}{\partial x}\right)_\beta \tag{33}$$

as would be expected.

The metric coefficient h_2 and distance along a streamline s are obtained by solving equations (20) and (23), respectively, as previously discussed.

Calculation of Heating Rates

Approximate three-dimensional heating rates along surface streamlines can be calculated through the axisymmetric analogue using any available axisymmetric boundary-layer solution. Although heating rates are usually calculated from a solution of the complete axisymmetric boundary-layer equations (eqs. (7) to (10)), this is unnecessary because very accurate results can be obtained more easily from approximate heat-transfer relations similar to those presented in reference 25. Following the nomenclature of reference 25, the expression for the heating rate to the surface is given by the following equation (see appendix C for details):

$$q_w = \left[\frac{H_e (\rho\mu)_w u_e h_2}{N_{Pr,w}\sqrt{2\bar{\xi}}}\right]\zeta'_w \tag{34}$$

where the transformed surface distance $\bar{\xi}$ is given by

$$\bar{\xi} = \int_0^s (\rho\mu)_w u_e h_2^2 \, ds \tag{35}$$

The parameter ζ_w' is the derivative of the nondimensional enthalpy profile normal to the wall $\left[\dfrac{\partial (H/H_e)}{\partial \bar{\eta}}\right]_w$ and is approximated by the expression (see appendix C)

$$\zeta_w' = 0.47 \left\{ \left[1.48 - 0.23 \left(\frac{\rho_e \mu_e}{\rho_w \mu_w} \right) \right] \left(\frac{\rho_e \mu_e}{\rho_w \mu_w} \right)^{1/2} \right\}$$

$$\times \left(N_{Pr} \left[1 - 0.24 N_{Pr} (1 - t_e)^2 \right] \right) \left(1 + 0.11 \sqrt{\bar{\beta}} \right) (\zeta_{aw} - \zeta_w) \tag{36}$$

where the velocity gradient parameter $\bar{\beta}$, the nondimensional adiabatic wall enthalpy ζ_{aw}, and the recovery factor RF are given by the following expressions:

$$\bar{\beta} = \frac{2\bar{\xi} \left(\dfrac{du_e}{ds} \right)}{t_e (\rho\mu)_w (u_e h_2)^2} \tag{37}$$

$$\zeta_{aw} = RF + (1 - RF) t_e \tag{38}$$

and

$$RF = \sqrt{N_{Pr}} \tag{39}$$

The approximate expression for ζ_w' (eq. (36)) has been found to predict values that agree with exact similar solutions (tabulated in ref. 26) to within ±4 percent for the following range of conditions:

16

$$0.1835 \leqq \left(\frac{\rho_e \mu_e}{\rho_w \mu_w}\right) \leqq 1.385 \tag{40a}$$

$$0.2 \leqq t_e \leqq 1.0 \tag{40b}$$

$$0.0076 \leqq \zeta_w \leqq 0.75 \tag{40c}$$

$$0 \leqq \bar{\beta} \leqq 3.5 \tag{40d}$$

Boundary-layer edge properties for the heat-transfer calculation are obtained by assuming that the flow expands isentropically along an inviscid surface streamline from the stagnation pressure to the local pressure obtained from the inviscid solution. Thus, the properties at the edge of the boundary layer (which are assumed equal to the inviscid wall conditions) can be expressed for a perfect gas as follows:

$$\rho_e = \rho_s (p_e/p_s)^{1/\gamma} \tag{41}$$

$$h_e = \frac{p_e}{\rho_e}\left(\frac{\gamma}{\gamma - 1}\right) \tag{42}$$

and

$$u_e = \sqrt{2(H_e - h_e)} \tag{43}$$

The wall temperature is assumed to be known; thus, the nondimensional enthalpy ratio at the wall can be calculated from the equation

$$\zeta_w = c_p T_w/H_e \tag{44}$$

The viscosity ratio μ_w/μ_e is computed from the Sutherland viscosity formula (ref. 27)

$$\frac{\mu_w}{\mu_e} = \left[\frac{1 + (S/T_e)}{(T_w/T_e) + (S/T_e)}\right]\left(\frac{T_w}{T_e}\right)^{3/2} \tag{45}$$

17

where S is a dimensional constant defined in the present work as

$$S = 110.33 \text{ K} \tag{46}$$

RESULTS AND DISCUSSION

In the sections that follow, the limitations and range of applicability of the method will be discussed; also, a comparison of calculated heating rates with experimental measurements for a spherically blunted 15° half-angle cone, a spherically blunted 80° sweep slab delta wing, and a Space Shuttle Orbiter type configuration will be presented.

Limitations and Range of Applicability

The basic assumption of the axisymmetric analogue is that the cross flow in the boundary layer is small (ref. 9). It has been shown that the cross flow in the boundary layer will be small when the streamline curvature on the surface is small (ref. 10) or when the wall is highly cooled (ref. 11). The first condition is rather restrictive since in general it will be satisfied only for smooth bodies (that is, bodies with only small changes in curvature) at small angle of attack. The second condition is less restrictive because for many applications the wall temperature is only a small fraction of the adiabatic wall temperature. However, these conditions are both qualitative and it is necessary to compare calculated heating rates with experimental data to validate the theory.

In the present paper, it is assumed that the Reynolds number is large enough for boundary-layer concepts to apply but not large enough to cause transition to turbulent flow. The first of these assumptions is necessary since the concept of the axisymmetric analogue is based on boundary-layer theory. The second assumption is not necessary since Cooke and Hall (ref. 13) have shown that the axisymmetric analogue can be extended to turbulent flows. However, turbulent flows are not considered in the present paper.

Further, it has been assumed that the boundary layer follows inviscid surface streamline paths and that the entropy of the fluid at the edge of the boundary layer is constant. This is equivalent to assuming that the boundary layer is very thin and that all of the fluid entering the boundary layer has passed through the normal portion of the bow shock wave. This is a good assumption in the nose region and for some distance downstream of the nose for high Reynolds number laminar flow.

In the region far downstream of the nose, the boundary-layer thickness is no longer negligible, and the entropy of the fluid entering the boundary layer is not constant. In this region, it becomes increasingly important to account for boundary-layer growth in calculating the metric coefficient h_2 and variable entropy in calculating boundary-layer edge conditions, both of which can have a strong influence on heating rates. These effects have not been considered in the present paper because they would unnecessarily complicate the devel-

opment of the method and are considered of small importance for the experimental comparisons which follow. These effects can be incorporated in the heating calculations at some future time.

Comparisons With Experimental Data

Spherically blunted 15° half-angle cone.- Calculated heating rates are compared with experimental measurements from reference 28 on a spherically blunted 15° half-angle cone at angles of attack of 0°, 10°, and 20°. The experimental tests (ref. 28) were performed in air (γ = 1.4) at a free-stream Mach number of 10.6 and a free-stream unit Reynolds number of 1.31 × 10^6 per meter. The ratio of wall to boundary-layer edge stagnation enthalpy ζ_w for these tests was 0.27. The Prandtl number was assumed to be 0.72.

The α = 0° case is of particular interest because the flow is axisymmetric and results obtained by the present theory can be compared with other theoretical results. First, it is well-known that the metric coefficient which describes the divergence or convergence of streamlines in axisymmetric boundary-layer flows is equal to the body cross-sectional radius (refs. 20 and 29). To check this result, the metric coefficient obtained from the present theory for this case is compared with the body cross-sectional radius in figure 9. The results for the nose region ($x/R_n \leqq 2$) are presented in figure 9(a) and the downstream region ($x/R_n \geqq 2$) in figure 9(b). As would be expected for any axisymmetric body at α = 0°, the calculated metric coefficient h_2 agrees almost exactly with the body radius r_b.

The axial distribution of heat-transfer rate for α = 0° is presented in figure 10. The present theory is compared with experimental data from reference 28 and the results of a nonsimilar axisymmetric boundary layer solution computed by the method of reference 21. Both calculated results are in very good agreement with the experimental data. The approximate heat-transfer relations used in the present theory (eqs. (34) to (39)) yield results comparable to those obtained using the differential boundary-layer solution procedure (ref. 21).

The axial heat-transfer distributions along two meridional planes - the windward symmetry plane (Φ = -90°) and the side meridional plane (Φ = 0°) - are presented in figure 11 for an angle of attack of 10°. Experimental data from reference 28 for two different nose bluntness are presented for comparison. The calculated heating rates are in good agreement with the experimental data along each meridional plane although there is considerable scatter in the experimental measurements in the windward symmetry plane (Φ = -90°) for values of x/R_n greater than about 12.

The circumferential heating distributions for α = 10° are presented in figure 12 at two axial stations: x/R_n = 3.1 and x/R_n = 12.0. The abscissa for each part of the figure begins in the windward symmetry plane (Φ = -90°) and continues around to the leeward symmetry plane (Φ = 90°). Heating rates calculated by the present method agree well with the experimental data around the cone at each axial station.

The axial heating-rate distributions at $\alpha = 20°$ are presented in figure 13, and the circumferential heating-rate distributions for this angle of attack are presented in figure 14. The calculated heating rates are in good agreement with the experimental data in each instance. These good comparisons are very encouraging because the inviscid surface streamlines for this angle of attack (see fig. 15) exhibit large divergence over much of the lower surface and side of the cone. This suggests that the small cross-flow analogy can yield reasonably accurate heat-transfer results even in regions of relatively large streamline divergence for values of ζ_w as large as 0.27.

In all of the theoretical results presented previously the pole of the local polar coordinate system has been coincident with the body axis. Thus, $r_0(x)$ is equal to zero; and since the geometry is axisymmetric, $\partial R_b / \partial \Phi$ is also equal to zero. This greatly simplifies the problem since many of the terms drop out of the equations and may have the effect of masking errors in the program that would show up later for more complicated geometries. Thus, the inviscid flow-field and heat-transfer calculations were repeated using the shifted pole configuration defined by the following expressions:

For $0 \leq x \leq 1.5$,

$$r_0(x) = 0$$

For $1.5 \leq x \leq 15.0$,

$$r_0(x) = -0.13991(x - 1.5)$$

which is illustrated in figure 16. The calculations were performed for $\alpha = 0°$ and $10°$, and the results are compared with previous heat-transfer calculations in figures 17 to 19. The heating rates obtained using the shifted-pole configuration agree closely with those obtained previously when the pole was aligned with the body axis (i.e., $r_0(x) = 0$). With these results, heating rates on more complicated body geometries can be computed with added confidence.

Spherically blunted 80° sweep slab delta wing.- Next, calculated heat-transfer coefficients are compared with experimental measurements, from reference 30, on a spherically blunted 80° sweep slab delta wing (fig. 20) at angles of attack of 0°, 10°, and 20°. The experimental tests in reference 30 were performed in air ($\gamma = 1.4$) at a free-stream Mach number of 9.6 and a free-stream unit Reynolds number of 3.94×10^6 per meter. The ratio of wall to boundary-layer edge stagnation enthalpy ζ_w in the tests was 0.33, and the Prandtl number was assumed to be 0.72.

The axial distribution of heat-transfer coefficients for $\alpha = 0°$ is presented in figure 21. The heat-transfer coefficients calculated by the present theory are seen to be in good agreement with the experimental data.

The circumferential distributions of heat-transfer coefficient for $\alpha = 0^\circ$ are presented in figure 22 at three stations ($l/R_n = 4$, 8, and 12) measured from the beginning of the wing leading edge. These distributions were obtained along cross-sectional cuts normal to the wing leading edge (i.e., the dashed lines in figure 20). Even at $\alpha = 0^\circ$, the heating about a delta wing is not axisymmetric because of the geometry; but it is symmetric about the wing leading edge ($\Phi = 0^\circ$). At the upstream station, $l/R_n = 4$, the present theory underpredicts the experimental data slightly around the leading edge; but at the two down-stream stations, $l/R_n = 8$ and 12, the theory is in very good agreement with the data.

The axial distribution of heat-transfer coefficient at $\alpha = 10^\circ$ is pre-sented in figure 23. As at the lower angle of attack, the heat-transfer coef-ficients calculated by the present theory are in very good agreement with the experimental data. Circumferential distributions at this angle of attack are presented in figure 24. At each station, the heating increases in a direction away from the windward symmetry plane ($\Phi = -90^\circ$) until it reaches a peak slightly ahead of the wing leading edge ($\Phi < 0^\circ$) and then decreases rapidly around the leading edge on the lee side. The heat-transfer calculations do not extend all the way around to the leeward symmetry plane ($\Phi = 90^\circ$) because a cross-flow shock wave occurs in the inviscid flow field solution on the lee side of the body, and the boundary-layer equations cannot be used to accurately com-pute the heating in this region. Heat-transfer coefficients predicted by the present theory are generally in good agreement with the experimental data. The most notable exception occurs near peak heating for $l/R_n = 12$; however, the experimental data point in this region takes an inexplicable dip and may be in error.

The axial distribution of heat-transfer coefficients at $\alpha = 20^\circ$ is pre-sented in figure 25. It can be noted that the present theory is in good agree-ment with the experimental data. The circumferential distributions at this angle of attack are presented in figure 26. The heating at this higher angle of attack is qualitatively similar to the heating at $\alpha = 10^\circ$, except the level on the windward side and leading-edge region is much higher. Again, it is found that the present theory is in good overall agreement with the experimental data.

The inviscid surface streamlines for the delta wing at $\alpha = 0^\circ$ are pre-sented in figure 27. There is one streamline that lies in the wing leading-edge symmetry plane (fig. 27(a)) which divides the streamline pattern into a symmet-rical upper and lower part. Near the bottom symmetry plane (fig. 27(b)) where the heating is low, the streamlines have very little curvature. However, on the wing leading edge (fig. 27(a)) where the heating is relatively high, the stream-lines diverge very rapidly.

The overall agreement between the predicted and measured heating rates on the blunt-slab delta wing is very good. This is the first time that three-dimensional heating rates on a blunt-slab delta wing have been calculated suc-cessfully. This is very encouraging because this configuration is not axisym-metric and, although analytic, has many features that are similar to more complicated vehicles.

Space Shuttle Orbiter type configuration.- Finally, calculated heat-transfer coefficients on a Space Shuttle Orbiter type configuration are compared with experimental measurements from reference 31 at angles of attack of 20°and 25°. The experimental tests in reference 31 were performed in air (γ = 1.4) at a free-stream Mach number of 7.9 and a free-stream unit Reynolds number of 1.64 × 10^6 per meter. The ratio of wall to boundary-layer edge stagnation enthalpy ζ_w for the tests was 0.31, and the Prandtl number was assumed to be 0.72. The model used in the experimental tests was 0.0175-scale model of the full-scale vehicle shown in figure 28.

In constructing the mathematical geometry model from the QUICK geometry program to use in the inviscid flow field calculations, the canopy was faired smooth as shown by the dashed line in figure 28, and the vertical tail and reaction jet control pod on the rear of the vehicle were omitted. Difficulties were encountered when computing the lee-side flow field with the "realistic" cross-sectional geometry; thus the lee-side cross section was smoothed out using an elliptical segment. (See dashed line in section A-A of fig. 28.) The lower side of the vehicle geometry was accurately modeled so that the flow on the windward surface could be accurately computed. The modifications to the lee-side geometry had no effect on the windward-side flow calculations because in all cases the cross-flow velocity went supersonic before the geometry modifications were encountered. The inviscid solutions were computed over the forward 60 percent of the vehicle length, back to where the wing started to flare out rapidly. (See dashed line in top view of fig. 28.) At this point, the axial velocity at the wing tip became subsonic and the solution could not proceed farther downstream. (See discussion of limitations of supersonic marching techniques in refs. 17 and 19.) Thus, the heating rates could only be computed on approximately the forward 60 percent of the windward side.

The axial distribution of heat-transfer coefficient along the windward symmetry plane at α = 20° is presented in figure 29. As can be noted, the heat-transfer coefficients calculated by the present theory are in very good agreement with the experimental data.

Lateral distributions of heat-transfer coefficient across the lower surface of the model at α = 20° are presented in figure 30 for two axial stations: x/L = 0.4 and x/L = 0.5. The calculated heat-transfer coefficients are in very good agreement with the few experimental data points that are available. Although no data are available near peak heating, the excellent results noted previously for the delta wing in this region lend confidence to the present predictions.

For α = 25°, axial distributions of heat-transfer coefficient are presented in figure 31, and lateral distributions are presented in figure 32. As at the lower angle of attack, the present theory is in very good agreement with the experimental data.

The inviscid surface streamlines on the windward surface of the Space Shuttle Orbiter type configuration are presented in figure 33. It should be noted that near the symmetry plane where the heating rates are relatively low the streamlines have little curvature; whereas at the outer edge of the body where

the heating rates increase sharply, the streamline curvature also increases rapidly - as would be expected.

Thus, on the windward surface of a Space Shuttle Orbiter type configuration where the inviscid flow field can be accurately computed the present theory has been shown to predict heating rates that are in very good overall agreement with experimental data at moderately high angles of attack.

From the present study, it appears that accurate three-dimensional heating rates can be computed on most regions of a vehicle where boundary-layer concepts apply if ζ_w is not too large (i.e., less than approximately 0.4) and an accurate inviscid flow field solution can be computed. The range of ζ_w might be extended even higher through future comparisons with other experimental data. From the experience gained in the present study it is estimated that the heating over a "complete" vehicle can be obtained in a few minutes computing time on a Control Data CYBER 175 (or equivalent) computer once the inviscid flow field has been obtained. Consequently, the present theory should prove very useful in studying the heating on advanced Earth entry vehicles.

CONCLUDING REMARKS

A theoretical method has been developed for computing approximate laminar heating rates on three-dimensional configurations at angle of attack. The method is based on the axisymmetric analogue which is used to reduce the three-dimensional boundary-layer equations along streamlines to an equivalent axisymmetric form by using the metric coefficient which describes streamline divergence (or convergence). The method has been coupled with a three-dimensional inviscid flow field program for computing surface streamline paths, metric coefficients, and boundary-layer edge conditions. Using this method, accurate laminar heating rates can be computed for a wide range of three-dimensional configurations at moderately large angles of attack. This conclusion is supported by good comparisons with experimental data on a spherically blunted 15° half-angle cone, a spherically blunted 80° sweep slab delta wing, and a Space Shuttle Orbiter type configuration at angles of attack up to 25°. Computations proceed very rapidly with the heating calculations for a complete configuration requiring only a few minutes of computing time.

Langley Research Center
National Aeronautics and Space Administration
Hampton, VA 23665
July 15, 1980

TRANSFORMATION FROM CYLINDRICAL COORDINATES

TO LOCAL POLAR COORDINATES

The equations relating local polar coordinates and cylindrical coordinates are given by equations (17a) to (17d)

$$r_b = R_b\sqrt{\bar{A}^2 + 1} \, \cos \, \Phi \tag{A1}$$

$$\phi = \tan^{-1} \, (\bar{A}) \tag{A2}$$

$$x = \chi \tag{A3}$$

where

$$\bar{A} = \tan \, \Phi + r_0(\chi)/(R_b \, \cos \, \Phi) \tag{A4}$$

The transformation operators for transforming derivatives from cylindrical coordinates on a surface (ϕ, x) to local polar coordinates on a surface (Φ, χ) are

$$\left(\frac{\partial}{\partial\phi}\right)_x = \left(\frac{\partial\Phi}{\partial\phi}\right)_x\left(\frac{\partial}{\partial\Phi}\right)_\chi + \left(\frac{\partial\chi}{\partial\phi}\right)_x\left(\frac{\partial}{\partial\chi}\right)_\Phi \tag{A5}$$

$$\left(\frac{\partial}{\partial x}\right)_\phi = \left(\frac{\partial\Phi}{\partial x}\right)_\phi\left(\frac{\partial}{\partial\Phi}\right)_\chi + \left(\frac{\partial\chi}{\partial x}\right)_\phi\left(\frac{\partial}{\partial\chi}\right)_\Phi \tag{A6}$$

Now since

$$\left(\frac{\partial\chi}{\partial\phi}\right)_x = 0$$

and

$$\left(\frac{\partial \chi}{\partial x}\right)_\phi = 1$$

equations (A5) and (A6) can be written as

$$\left(\frac{\partial}{\partial \phi}\right)_x = \left(\frac{\partial \Phi}{\partial \phi}\right)_x \left(\frac{\partial}{\partial \Phi}\right)_\chi \tag{A7}$$

and

$$\left(\frac{\partial}{\partial x}\right)_\phi = \left(\frac{\partial \Phi}{\partial x}\right)_\phi \left(\frac{\partial}{\partial \Phi}\right)_\chi + \left(\frac{\partial}{\partial \chi}\right)_\Phi \tag{A8}$$

Similarly, the reverse transformation operators are

$$\left(\frac{\partial}{\partial \Phi}\right)_\chi = \left(\frac{\partial \phi}{\partial \Phi}\right)_\chi \left(\frac{\partial}{\partial \phi}\right)_x \tag{A9}$$

$$\left(\frac{\partial}{\partial \chi}\right)_\Phi = \left(\frac{\partial \phi}{\partial \chi}\right)_\Phi \left(\frac{\partial}{\partial \phi}\right)_x + \left(\frac{\partial}{\partial x}\right)_\phi \tag{A10}$$

Now solving equation (A9) for $\left(\dfrac{\partial}{\partial \phi}\right)_x$ the following result is obtained:

$$\left(\frac{\partial}{\partial \phi}\right)_x = \frac{1}{\left(\dfrac{\partial \phi}{\partial \Phi}\right)_\chi} \left(\frac{\partial}{\partial \Phi}\right)_\chi \tag{A11}$$

Comparison of equations (A7) and (A11) shows that

$$\left(\frac{\partial \Phi}{\partial \phi}\right)_x = \frac{1}{\left(\frac{\partial \phi}{\partial \Phi}\right)_\chi} \tag{A12}$$

Similarly, solving equation (A10) for $\left(\frac{\partial}{\partial x}\right)_\phi$ and using equation (A11) to

replace $\left(\frac{\partial}{\partial \phi}\right)_x$ results in

$$\left(\frac{\partial}{\partial x}\right)_\phi = -\left[\frac{\left(\frac{\partial \phi}{\partial \chi}\right)_\Phi}{\left(\frac{\partial \phi}{\partial \Phi}\right)_\chi}\right]\left(\frac{\partial}{\partial \Phi}\right)_\chi + \left(\frac{\partial}{\partial \chi}\right)_\Phi \tag{A13}$$

Comparing equation (A10) with equation (A13) gives

$$\left(\frac{\partial \Phi}{\partial x}\right)_\phi = -\left[\frac{\left(\frac{\partial \phi}{\partial \chi}\right)_\Phi}{\left(\frac{\partial \phi}{\partial \Phi}\right)_\chi}\right] \tag{A14}$$

The derivatives $\left(\frac{\partial \phi}{\partial \Phi}\right)_\chi$ and $\left(\frac{\partial \phi}{\partial \chi}\right)_\Phi$ can be obtained from equation (A2) as

follows:

$$\left(\frac{\partial \phi}{\partial \Phi}\right)_\chi = \left(\frac{\partial}{\partial \Phi}\right)_\chi (\tan^{-1} \bar{A}) \tag{A15}$$

or

$$\left(\frac{\partial\phi}{\partial\Phi}\right)_\chi = \frac{1}{1 + \bar{A}^2}\left(\frac{\partial\bar{A}}{\partial\Phi}\right)_\chi \tag{A16}$$

Similarly,

$$\left(\frac{\partial\phi}{\partial\chi}\right)_\Phi = \frac{1}{1 + \bar{A}^2}\left(\frac{\partial\bar{A}}{\partial\chi}\right)_\Phi \tag{A17}$$

From equation (A4), the following expressions can be obtained for the derivatives $\left(\dfrac{\partial\bar{A}}{\partial\Phi}\right)_\chi$ and $\left(\dfrac{\partial\bar{A}}{\partial\chi}\right)_\Phi$, respectively:

$$\left(\frac{\partial\bar{A}}{\partial\Phi}\right)_\chi = \frac{1}{R_b^2 \cos^2\Phi}\left\{R_b^2 + r_0\left[R_b \sin\Phi - \left(\frac{\partial R_b}{\partial\Phi}\right)_\chi \cos\Phi\right]\right\} \tag{A18}$$

$$\left(\frac{\partial\bar{A}}{\partial\chi}\right)_\Phi = \frac{1}{R_b \cos\Phi}\left[\frac{dr_0}{d\chi} - \frac{r_0}{R_b}\left(\frac{\partial R_b}{\partial\chi}\right)_\Phi\right] \tag{A19}$$

Combining equations (A16) and (A18) gives the following expression for $\left(\dfrac{\partial\phi}{\partial\Phi}\right)_\chi$:

$$\left(\frac{\partial\phi}{\partial\Phi}\right)_\chi = \frac{R_b^2 + r_0\left[R_b \sin\Phi - \left(\dfrac{\partial R_b}{\partial\Phi}\right)_\chi \cos\Phi\right]}{\left(1 + \bar{A}^2\right)\left(R_b^2 \cos^2\Phi\right)} \tag{A20}$$

Similarly, from equations (A17) and (A19),

$$\left(\frac{\partial \phi}{\partial \chi}\right)_{\Phi} = \frac{\dfrac{dr_0}{d\chi} - \dfrac{r_0}{R_b}\left(\dfrac{\partial R_b}{\partial \chi}\right)_{\Phi}}{\left(1 + \bar{A}^2\right)(R_b \cos \Phi)} \tag{A21}$$

From equations (A12) and (A20),

$$\left(\frac{\partial \Phi}{\partial \phi}\right)_x = \frac{\left(1 + \bar{A}^2\right)\left(R_b^2 \cos^2 \Phi\right)}{R_b^2 + r_0\left[R_b \sin \Phi - \left(\dfrac{\partial R_b}{\partial \Phi}\right)_\chi \cos \Phi\right]} \tag{A22}$$

Similarly, from equations (A14), (A20), and (A21),

$$\left(\frac{\partial \Phi}{\partial x}\right)_\phi = -R_b \cos \Phi\left\{\frac{\dfrac{dr_0}{d\chi} - \dfrac{r_0}{R_b}\left(\dfrac{\partial R_b}{\partial \chi}\right)_\Phi}{R_b^2 + r_0\left[R_b \sin \Phi - \left(\dfrac{\partial R_b}{\partial \Phi}\right)_\chi \cos \Phi\right]}\right\} \tag{A23}$$

In summary, the transformation operators defined by equations (A7) and (A8) can be used with equation (A22) which defines $\left(\dfrac{\partial \Phi}{\partial \phi}\right)_x$ and equation (A23) which defines $\left(\dfrac{\partial \Phi}{\partial x}\right)_\phi$ to transform derivatives from cylindrical coordinates to local polar coordinates. The quantities R_b, r_0, $\dfrac{dr_0}{d\chi}$, $\left(\dfrac{\partial R_b}{\partial \Phi}\right)_\chi$, and $\left(\dfrac{\partial R_b}{\partial \chi}\right)_\Phi$ used in the previous equations must be obtained from the geometry description program.

These operators will now be used to transform the equations for the body geometry angles δ_ϕ and Γ from cylindrical coordinates to local polar coordinates. First, consider δ_ϕ which is given by equation (21)

28

$$\tan \delta_\phi = \frac{1}{r_b}\left(\frac{\partial r_b}{\partial \phi}\right)_x \tag{A24}$$

Using equation (A7), the derivative $\left(\frac{\partial r_b}{\partial \phi}\right)_x$ can be written as

$$\left(\frac{\partial r_b}{\partial \phi}\right)_x = \left(\frac{\partial \Phi}{\partial \phi}\right)_x \left(\frac{\partial r_b}{\partial \Phi}\right)_\chi \tag{A25}$$

From equation (A1),

$$\left(\frac{\partial r_b}{\partial \Phi}\right)_\chi = R_b \sqrt{1 + \bar{A}^2} \cos \Phi \left[\frac{1}{R_b}\left(\frac{\partial R_b}{\partial \Phi}\right)_\chi + \frac{\bar{A}}{1 + \bar{A}^2}\left(\frac{\partial \bar{A}}{\partial \Phi}\right)_\chi - \tan \Phi\right] \tag{A26}$$

Substituting this result into equation (A24) and using equation (A1) gives

$$\tan \delta_\phi = \frac{\left(\frac{\partial \Phi}{\partial \phi}\right)_x \left(\frac{\partial r_b}{\partial \Phi}\right)_\chi}{R_b \sqrt{1 + \bar{A}^2} \cos \Phi} \tag{A27}$$

where $\left(\frac{\partial \Phi}{\partial \phi}\right)_x$ is given by equation (A22) and $\left(\frac{\partial r_b}{\partial \Phi}\right)_\chi$ is given by equation (A26).

Next, consider Γ which is given by equation (22)

$$\tan \Gamma = \cos \delta_\phi \left(\frac{\partial r_b}{\partial x}\right)_\phi \tag{A28}$$

From equation (A8), the derivative $\left(\dfrac{\partial r_b}{\partial x}\right)_\phi$ can be written as

$$\left(\frac{\partial r_b}{\partial x}\right)_\phi = \left(\frac{\partial \Phi}{\partial x}\right)_\phi \left(\frac{\partial r_b}{\partial \Phi}\right)_\chi + \left(\frac{\partial r_b}{\partial \chi}\right)_\Phi \tag{A29}$$

From equation (A1),

$$\left(\frac{\partial r_b}{\partial \chi}\right)_\Phi = R_b \sqrt{1 + \bar{A}^2} \cos \Phi \left[\frac{1}{R_b}\left(\frac{\partial R_b}{\partial \chi}\right)_\Phi + \frac{\bar{A}}{1 + \bar{A}^2}\left(\frac{\partial \bar{A}}{\partial \chi}\right)_\Phi \right] \tag{A30}$$

Substituting equation (A29) into equation (A28) yields

$$\tan \Gamma = \cos \delta_\phi \left[\left(\frac{\partial \Phi}{\partial x}\right)_\phi \left(\frac{\partial r_b}{\partial \Phi}\right)_\chi + \left(\frac{\partial r_b}{\partial \chi}\right)_\Phi \right] \tag{A31}$$

where $\left(\dfrac{\partial \Phi}{\partial x}\right)_\phi$ is given by equation (A23), $\left(\dfrac{\partial r_b}{\partial \Phi}\right)_\chi$ is given by equation (A26), and $\left(\dfrac{\partial r_b}{\partial \chi}\right)_\Phi$ is given by equation (A29).

Next, consider the transformation of the equation describing the streamline location (eq. (19)):

$$\left(\frac{\partial \phi}{\partial x}\right)_\beta = \frac{1}{r_b}\left(\frac{\tan \theta \cos \delta_\phi}{\cos \Gamma} - \tan \Gamma \sin \delta_\phi\right) \tag{A32}$$

from cylindrical coordinates ϕ, x to local polar coordinates Φ, χ. Using equations (A2) and (A4), the following are obtained:

$$\left(\frac{\partial \phi}{\partial x}\right)_\beta = \frac{1}{1 + \bar{A}^2}\left(\frac{\partial \bar{A}}{\partial x}\right)_\beta \tag{A33}$$

and

$$\left(\frac{\partial \bar{A}}{\partial x}\right)_\beta = \left(\frac{R_b + r_0 \sin \Phi}{R_b \cos^2 \Phi}\right)\left(\frac{\partial \Phi}{\partial x}\right)_\beta + \frac{1}{R_b \cos \Phi}\left[\left(\frac{\partial r_0}{\partial x}\right)_\beta - \frac{r_0}{R_b}\left(\frac{\partial R_b}{\partial x}\right)_\beta\right] \tag{A34}$$

Now, combining equations (A33) and (A34) and solving for $\left(\dfrac{\partial \Phi}{\partial \chi}\right)_\beta$ yields

$$\left(\frac{\partial \Phi}{\partial \chi}\right)_\beta = \left(\frac{\partial \Phi}{\partial x}\right)_\beta = \left(1 + \bar{A}^2\right)\left(\frac{R_b \cos^2 \Phi}{R_b + r_0 \sin \Phi}\right)\left\{\left(\frac{\partial \phi}{\partial x}\right)_\beta\right.$$

$$\left. + \frac{1}{R_b \cos \Phi}\left[\frac{r_0}{R_b}\left(\frac{\partial R_b}{\partial x}\right)_\beta - \left(\frac{\partial r_0}{\partial x}\right)_\beta\right]\right\} \tag{A35}$$

Next, changing from an x, β coordinate system to an x, ϕ coordinate system,

$$\left(\frac{\partial}{\partial x}\right)_\beta = \left(\frac{\partial}{\partial x}\right)_\phi + \left(\frac{\partial \phi}{\partial x}\right)_\beta \left(\frac{\partial}{\partial \phi}\right)_x \tag{A36}$$

Further, using equations (A7) and (A8),

$$\left(\frac{\partial}{\partial x}\right)_\beta = \left(\frac{\partial \phi}{\partial x}\right)_\beta \left[\left(\frac{\partial \Phi}{\partial \phi}\right)_x \left(\frac{\partial}{\partial \Phi}\right)_\chi\right] + \left[\left(\frac{\partial \Phi}{\partial x}\right)_\phi \left(\frac{\partial}{\partial \Phi}\right)_\chi + \left(\frac{\partial}{\partial \chi}\right)_\Phi\right] \tag{A37}$$

or rearranging terms,

$$\left(\frac{\partial}{\partial x}\right)_\beta = \left[\left(\frac{\partial \phi}{\partial x}\right)_\beta \left(\frac{\partial \Phi}{\partial \phi}\right)_x + \left(\frac{\partial \Phi}{\partial x}\right)_\phi\right]\left(\frac{\partial}{\partial \Phi}\right)_\chi + \left(\frac{\partial}{\partial \chi}\right)_\Phi \tag{A38}$$

Now, since $r_0 = r_0(\chi)$,

$$\left(\frac{\partial r_0}{\partial x}\right)_\beta = \left(\frac{\partial r_0}{\partial \chi}\right)_\Phi = \frac{dr_0}{d\chi} \tag{A39}$$

With the use of equation (A38), the following is obtained:

$$\left(\frac{\partial R_b}{\partial x}\right)_\beta = \left[\left(\frac{\partial \Phi}{\partial x}\right)_\phi + \left(\frac{\partial \phi}{\partial x}\right)_\beta\left(\frac{\partial \Phi}{\partial \phi}\right)_x\right]\left(\frac{\partial R_b}{\partial \Phi}\right)_\chi + \left(\frac{\partial R_b}{\partial \chi}\right)_\Phi \tag{A40}$$

where $\left(\frac{\partial \Phi}{\partial x}\right)_\phi$ is given by equation (A23), $\left(\frac{\partial \phi}{\partial x}\right)_\beta$ is given by equation (A32), $\left(\frac{\partial \Phi}{\partial \phi}\right)_x$ is given by equation (A22), and $\left(\frac{\partial R_b}{\partial \Phi}\right)_\chi$ and $\left(\frac{\partial R_b}{\partial \chi}\right)_\Phi$ are given by the geometry description program QUICK.

APPENDIX B

CALCULATION OF SURFACE VELOCITY DIRECTION FROM

INVISCID SOLUTION

In order to integrate equation (30) to determine the location of a stream-line on the surface, it is necessary to know $\theta = \theta(\Phi, \chi)$. This must be obtained from a solution of the inviscid flow field. The solution is obtained using the STEIN (supersonic three-dimensional external inviscid) flow field code described in references 17 and 19. From the inviscid solution the Cartesian velocity components are known; these can then be used to determine the velocity direction θ on the surface.

Consider sketch (a), which shows the Cartesian velocity components w_1, w_2, and w_3, and sketch (b), which shows a cross-section plane normal to the body axis:
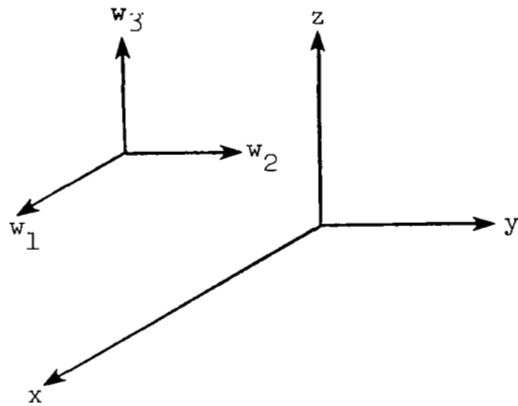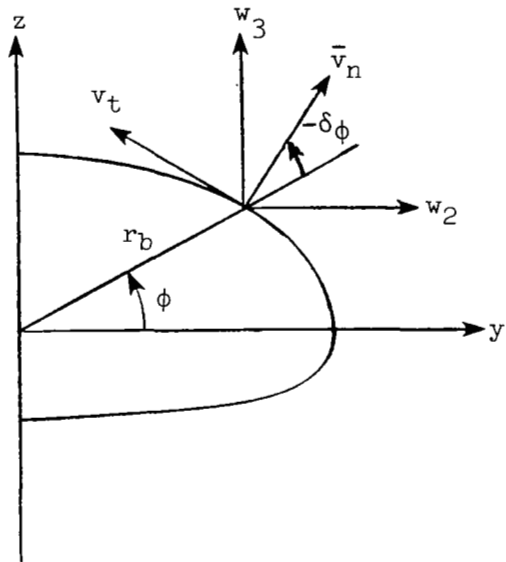
Sketch (a)   Sketch (b)

The velocity components v_t and $\bar{v}_n$ are given by the equations

$$v_t = w_3 \cos (\phi - \delta_\phi) - w_2 \sin (\phi - \delta_\phi) \tag{B1}$$

$$\bar{v}_n = w_3 \sin (\phi - \delta_\phi) + w_2 \cos (\phi - \delta_\phi) \tag{B2}$$

Now, in a plane parallel to the axis and normal to the body shown in sketch (c),
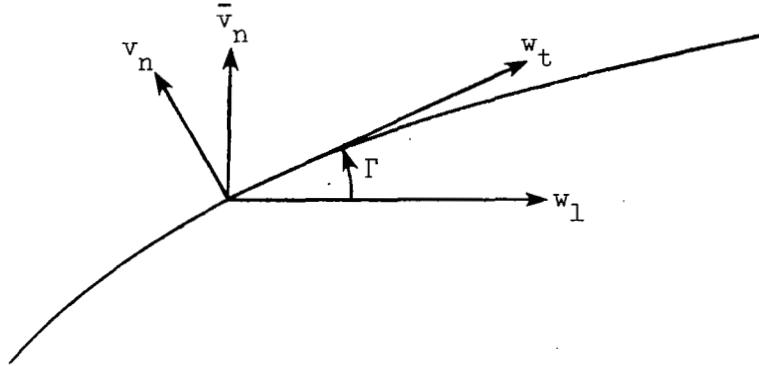
Sketch (c)

the velocity component tangent to the body w_t is given by the equation

$$w_t = \bar{v}_n \sin \Gamma + w_1 \cos \Gamma \tag{B3}$$

Finally, the streamline direction θ is given by the equation

$$\theta = \tan^{-1} (v_t/w_t) \tag{B4}$$

APPENDIX C

DEVELOPMENT OF EQUATIONS FOR CALCULATING

HEAT-TRANSFER RATE AT WALL

The heat-transfer rate to the wall q_w is given by the expression

$$q_w = k_w \left(\frac{\partial T}{\partial n}\right)_w \tag{C1}$$

where k is the thermal conductivity of the fluid and $\left(\frac{\partial T}{\partial n}\right)_w$ is the derivative of the temperature of the fluid normal to the wall. Equation (C1) can be rewritten in terms of the static enthalpy derivative as follows:

$$q_w = \frac{k_w}{c_{p,w}} \left(\frac{\partial h}{\partial n}\right)_w \tag{C2}$$

Neglecting cross flow in the boundary layer, the static enthalpy h is related to the total enthalpy H by the equation

$$h = H - \frac{u^2 + w^2}{2} \tag{C3}$$

Differentiating the terms in equation (C3) with respect to n yields

$$\frac{\partial h}{\partial n} = \frac{\partial H}{\partial n} - u \frac{\partial u}{\partial n} - w \frac{\partial w}{\partial n}$$

and since $u = w = 0$ at the wall,

$$\left(\frac{\partial h}{\partial n}\right)_w = \left(\frac{\partial H}{\partial n}\right)_w \tag{C4}$$

35

Substituting equation (C4) into (C2) yields

$$q_w = \frac{k_w}{c_{p,w}}\left(\frac{\partial H}{\partial n}\right)_w \qquad (C5)$$

Multiplying and dividing the right-hand side of equation (C5) by μ_w yields

$$q_w = \mu_w\left(\frac{k}{c_p\mu}\right)_w\left(\frac{\partial H}{\partial n}\right)_w = \frac{\mu_w}{N_{Pr,w}}\left(\frac{\partial H}{\partial n}\right)_w \qquad (C6)$$

The laminar boundary-layer equations are usually solved in a Levy-Lee type coordinate system $(\bar{\xi}, \bar{\eta})$ given by the following equations (ref. 25):

$$\bar{\xi} = \int_0^s (\rho\mu)_w u_e h_2^2 \, ds \qquad (C7)$$

$$\bar{\eta} = \frac{u_e h_2}{\sqrt{2\bar{\xi}}} \int_0^n \rho \, dn \qquad (C8)$$

Using these variables, equation (C6) can be transformed to the following form:

$$q_w = \frac{\mu_w}{N_{Pr,w}}\left(\frac{\partial \bar{\eta}}{\partial n}\right)_w\left(\frac{\partial H}{\partial \bar{\eta}}\right)_w = \frac{(\rho\mu)_w u_e h_2}{N_{Pr,w}\sqrt{2\bar{\xi}}}\left(\frac{\partial H}{\partial \bar{\eta}}\right)_w \qquad (C9)$$

The total enthalpy in equation (C9) can be nondimensionalized by multiplying and dividing the right-hand side by H_e (which is independent of $\bar{\eta}$) to obtain the following:

$$q_w = \left[\frac{H_e (\rho\mu)_w u_e h_2}{N_{Pr,w}\sqrt{2\bar{\xi}}}\right]\left[\frac{\partial (H/H_e)}{\partial \bar{\eta}}\right]_w \qquad (C10)$$

APPENDIX C

Now defining

$$\zeta_w' \equiv \left[\frac{\partial(H/H_e)}{\partial\bar{\eta}}\right]_w \tag{C11}$$

equation (C10) can be written as

$$q_w = \left[\frac{H_e(\rho\mu)_w u_e h_2}{N_{Pr,w}\sqrt{2\bar{\xi}}}\right]\zeta_w' \tag{C12}$$

which is the same as equation (34).

In reference 25 it was shown that ζ_w' could be approximated by the expression

$$\zeta_w' = 0.47\left(\frac{\rho_e\mu_e}{\rho_w\mu_w}\right)^{0.475}[1 - (1 - N_{Pr,w})(1 - t_e)]$$

$$\times \left(1 + 0.1\sqrt{\bar{\beta}t_e}\right)(1 - \zeta_w) \tag{C13}$$

where $\bar{\beta}$ is the velocity gradient parameter given by the equation

$$\bar{\beta} = \frac{2\bar{\xi}\left(\dfrac{du_e}{ds}\right)}{t_e(\rho\mu)_w(u_e h_2)^2} \tag{C14}$$

Equation (C13) predicts values of ζ_w' that agree with tabulated results from boundary-layer solutions presented in reference 26 to within ±10 percent for the following range of conditions:

$$0.1835 \leq \left(\frac{\rho_e\mu_e}{\rho_w\mu_w}\right) \leq 0.9367$$

37

$$0.2 \leqq t_e \leqq 1.0$$

$$0.0076 \leqq \zeta_w \leqq 0.75$$

$$0.5 \leqq \bar{\beta} \leqq 3.5$$

Thus, from equations (C12) and (C13), heating rates can be rapidly calculated from boundary-layer edge and wall parameters without having to solve the complete set of boundary-layer partial differential equations (7) to (10).

In the present study, it was found that a slightly more accurate prediction of ζ_w' could be obtained by using the following equation (same as eq. (36)):

$$\zeta_w' = 0.47 \left\{ \left[\left[1.48 - 0.23 \left(\frac{\rho_e \mu_e}{\rho_w \mu_w} \right) \right] \left(\frac{\rho_e \mu_e}{\rho_w \mu_w} \right)^{0.5} \right] \left\{ N_{Pr,w} \left[1 - 0.24 N_{Pr,w} (1 - t_e)^2 \right] \right\} \right.$$

$$\left. \times \left(1 + 0.11 \sqrt{\bar{\beta}} \right) (\zeta_{aw} - \zeta_w) \right. \tag{C15}$$

where ζ_{aw} is given by

$$\zeta_{aw} = RF + (1 - RF) t_e \tag{C16}$$

and the wall recovery factor RF for laminar flow is assumed to be

$$RF = \sqrt{N_{Pr,w}} \tag{C17}$$

Predicted values of ζ_w' from equation (C15) agree with results of the boundary-layer solutions presented in reference 26 to within approximately ±4 percent for the following range of conditions:

$$0.1835 \leqq \left(\frac{\rho_e \mu_e}{\rho_w \mu_w} \right) \leqq 1.385 \tag{C18a}$$

$$0.2 \leqq t_e \leqq 1.0 \tag{C18b}$$

$$0.0076 \leqq \zeta_w \leqq 0.75 \tag{C18c}$$

$$0 \leq \bar{\beta} \leq 3.5 \qquad \text{(C18d)}$$

A few typical comparisons are presented in table I.

The range of conditions over which equation (C15) has been correlated covers the range of experimental conditions of interest in the present study which are given for experimental data by the following:

$$0.6 \leq \left(\frac{\rho_e \mu_e}{\rho_w \mu_w}\right) \leq 1.1 \qquad \text{(C19a)}$$

$$0.4 \leq t_e \leq 1.0 \qquad \text{(C19b)}$$

$$0.27 \leq \zeta_w \leq 0.33 \qquad \text{(C19c)}$$

$$0 \leq \bar{\beta} \leq 0.7 \qquad \text{(C19d)}$$

Equations (C12) (or eq. (34)) and (C15) (or eq. (36)) have been used in the present study to provide a simple but accurate method of calculating heating rates along a surface streamline.

REFERENCES

1. Haefeli, Rudolph C.; Littler, Ernest G.; Hurley, John B.; and Winter, Martin G.: Technology Requirements for Advanced Earth-Orbital Transportation Systems - Final Report. NASA CR-2866, 1977.

2. Hepler, A. K.; and Bangsund, E. L.: Technology Requirements for Advanced Earth Orbital Transportation Systems. Volume 2: Summary Report. NASA CR-2879, 1978.

3. Peyret, Roger; and Viviand, Henri: Computation of Viscous Compressible Flows Based on the Navier-Stokes Equations. AGARD-AG-212, Sept. 1975.

4. Harris, Julius E.: Calculation of Three-Dimensional Compressible Laminar and Turbulent Boundary Layers - An Implicit Finite-Difference Procedure for Solving the Three-Dimensional Compressible Laminar, Transitional, and Turbulent Boundary-Layer Equations. Aerodynamic Analyses Requiring Advanced Computers - Part I, NASA SP-347, 1975, pp. 19-40.

5. Kendall, Robert M.; Bonnett, William S.; Nardo, Charles T.; and Abbett, Michael J.: Calculation of Three-Dimensional Compressible Laminar and Turbulent Boundary Flows - Three-Dimensional Compressible Boundary Layers of Reacting Gases Over Realistic Configurations. Aerodynamic Analyses Requiring Advanced Computers - Part I, NASA SP-347, 1975, pp. 77-99.

6. McLean, J. Douglas: Three-Dimensional Turbulent Boundary Layer Calculations for Swept Wings. AIAA Paper 77-3, Jan. 1977.

7. Cebeci, Tuncer; Kaups, Kalle; Ramsey, Judy; and Moser, Alfred: Calculation of Three-Dimensional Compressible Laminar and Turbulent Boundary Layers - Calculation of Three-Dimensional Compressible Boundary Layers on Arbitrary Wings. Aerodynamic Analyses Requiring Advanced Computers - Part I, NASA SP-347, 1975, pp. 41-76.

8. McLean, J. D.; and Randall, J. L.: Computer Program To Calculate Three-Dimensional Boundary Layer Flows Over Wings With Wall Mass Transfer. NASA CR-3123, 1979.

9. Cooke, J. C.: An Axially Symmetric Analogue for General Three-Dimensional Boundary Layers. R. & M. No. 3200, British A.R.C., 1961.

10. Hayes, Wallace D.: The Three-Dimensional Boundary Layer. NAVORD Rep. 1313 (NOTS 384), U.S. Naval Ord. Test Station, Inyokern (China Lake, Calif.), May 9, 1951.

11. Vaglio-Laurin, Roberto: Laminar Heat Transfer on Three-Dimensional Blunt Nosed Bodies in Hypersonic Flow. ARS J., vol. 29, no. 2, Feb. 1959, pp. 123-129.

12. Fannelop, Torstein K.: A Method of Solving the Three-Dimensional Laminar Boundary-Layer Equations With Application to a Lifting Re-Entry Body. AIAA J., vol. 6, no. 6, June 1968, pp. 1075-1084.

13. Cooke, J. C.; and Hall, M. G.: Boundary Layers in Three Dimensions. Boundary Layer Problems. Vol. 2 of Progress in Aeronautical Sciences, Antonio Ferri, D. Küchemann, and L. H. G. Sterne, eds., Macmillan Co., c.1962, pp. 221-282.

14. Cooke, J. C.; and Jones, O. K.: The Boundary Layer on a Townend Surface. Aeronaut. Q., vol. XVI, pt. 2, May 1965, pp. 145-158.

15. DeJarnette, Fred R.; and Hamilton, H. Harris: Inviscid Surface Streamlines and Heat Transfer on Shuttle-Type Configurations. J. Spacecr. & Rockets, vol. 10, no. 6, May 1973, pp. 314-321.

16. DeJarnette, Fred R.: Aerodynamic Heating on Complex Configurations. Technical Papers - Conference on Advanced Techology for Future Space Systems, May 1979, pp. 179-188. (Available as AIAA Paper 79-0891.)

17. Marconi, Frank; Salas, Manuel; and Yaeger, Larry: Development of a Computer Code for Calculating the Steady Super/Hypersonic Inviscid Flow Around Real Configurations. Volume I - Computational Technique. NASA CR-2675, 1976.

    Marconi, Frank; and Yaeger, Larry: Development of a Computer Code for Calculating the Steady Super/Hypersonic Inviscid Flow Around Real Configurations. Volume II - Code Description. NASA CR-2676, 1976.

18. Rakich, John V.; and Pegot, Eva B.: Flow Field and Heating on the Windward Side of the Space Shuttle Orbiter. Aerodynamic Analyses Requiring Advanced Computers - Part II, NASA SP-347, 1975, pp. 1377-1394.

19. Marconi, Frank; Yaeger, Larry; and Hamilton, H. Harris: Computation of High-Speed Inviscid Flows About Real Configurations. Aerodynamic Analyses Requiring Advanced Computers - Part II, NASA SP-347, 1975, pp. 1411-1455.

20. Pai, Shih-I: Viscous Flow Theory. I - Laminar Flow. D. Van Nostrand Co., Inc., c.1956.

21. Anderson, E. C.; and Lewis, C. H.: Laminar or Turbulent Boundary-Layer Flows of Perfect Gases or Reacting Gas Mixtures in Chemical Equilibrium. NASA CR-1893, 1971.

22. Hamilton, Hubbard Harris, II: A Theoretical Investigation of the Effect of Heat Transfer on Laminar Separation. M.S. Thesis, Virginia Polytech. Inst. & State Univ., 1969. (Available as NASA TM X-61814.)

23. Vachris, Alfred F., Jr.; and Yaeger, Larry S.: QUICK-GEOMETRY - A Rapid Response Method for Mathematically Modeling Configuration Geometry. Applications of Computer Graphics in Engineering, NASA SP-390, 1975, pp. 49-73.

24. Moretti, Gino; and Bleich, Gary: Three-Dimensional Flow Around Blunt Bodies. AIAA J., vol. 5, no. 9, Sept. 1967, pp. 1557-1562.

25. Zoby, Ernest V.: Approximate Relations for Laminar Heat-Transfer and Shear-Stress Functions in Equilibrium Dissociated Air. NASA TN D-4484, 1968.

26. Cohen, Nathaniel B.: Boundary-Layer Similar Solutions and Correlation Equations for Laminar Heat-Transfer Distribution in Equilibrium Air at Velocities up to 41,100 Feet Per Second. NASA TR R-118, 1961.

27. Ames Research Staff: Equations, Tables, and Charts for Compressible Flow. NACA Rep. 1135, 1953. (Supersedes NACA TN 1428.)

28. Cleary, Joseph W.: Effects of Angle of Attack and Bluntness on Laminar Heating-Rate Distributions of a 15° Cone at a Mach number of 10.6. NASA TN D-5450, 1969.

29. Schlichting, Hermann (J. Kestin, transl.): Boundary Layer Theory. Fourth ed. McGraw-Hill Book Co. Inc., c.1960.

30. Whitehead, Allen H.; and Dunavant, James C.: A Study of Pressure and Heat Transfer Over an 80° Sweep Slap Delta Wing in Hypersonic Flow. NASA TN D-2708, 1965.

31. Herrera, B. J.: Results From a Convective Heat Transfer Rate Distribution Test on a 0.0175 Scale Model (22-0) of the Rockwell International Vehicle 4 Space Shuttle Configuration in the AEDC-VKF Tunnel B (OH49B). Volume 1. NASA CR-147,626, 1976. Volume 2. NASA CR-147,627, 1976.

TABLE I.- COMPARISON OF VALUES OF ζ_w' FROM EQUATION (C15) WITH EXACT

SIMILAR BOUNDARY-LAYER SOLUTIONS FROM REFERENCE 26

$\dfrac{\rho_e \mu_e}{\rho_w \mu_w}$	t_e	ζ_w	N_{Pr}	$\bar{\beta}$	ζ_w'		Percent error
					Reference 26	Equation (C15)	
0.5122	1.0	0.152	0.709	0	0.2845	0.2755	−3.16
				.5	.3055	.2969	−2.82
				3.5	.3377	.3322	−1.63
.9149	1.0	.75	.735	0	.1013	.1049	3.55
				.5	.1141	.1130	−.96
				3.5	.1316	.1265	−3.88
1.3850	.2	.5	.699	0	.1518	.1479	−2.57
				1.0	.1697	.1641	−3.30
				3.4	.1817	.1778	−2.15
.2322	1.0	.0152	.709	0	.2230	.2256	1.17
				.5	.2399	.2431	1.33
				3.4	.2659	.2713	2.03
.2505	.8	.0152	.709	0	.2206	.2246	1.81
				.5	.2365	.2421	2.37
				3.2	.2616	.2688	2.75
.3462	.6	.03	.680	0	.2293	.2308	.65
				.5	.2454	.2487	1.34
				3.0	.2715	.2747	1.18
.6249	.4	.10	.768	0	.2891	.2940	1.69
				.5	.3099	.3169	2.26
				3.5	.3498	.3545	1.34
.3897	.8	.05	.768	0	.2871	.2877	.21
				.5	.3087	.3101	.45
				3.2	.3426	.3444	.53
.7931	.2	.10	.768	0	.2889	.2947	2.01
				.5	.3086	.3177	2.95
				3.5	.3518	.3554	1.02
.9367	.6	.50	.699	0	.1723	.1700	−1.33
				.5	.1882	.1832	−2.66
				3.5	.2118	.2050	−3.21
1.0810	.4	.50	.699	0	.1628	.1587	−2.52
				.5	.1763	.1711	−2.95
				3.5	.1978	.1914	−3.24
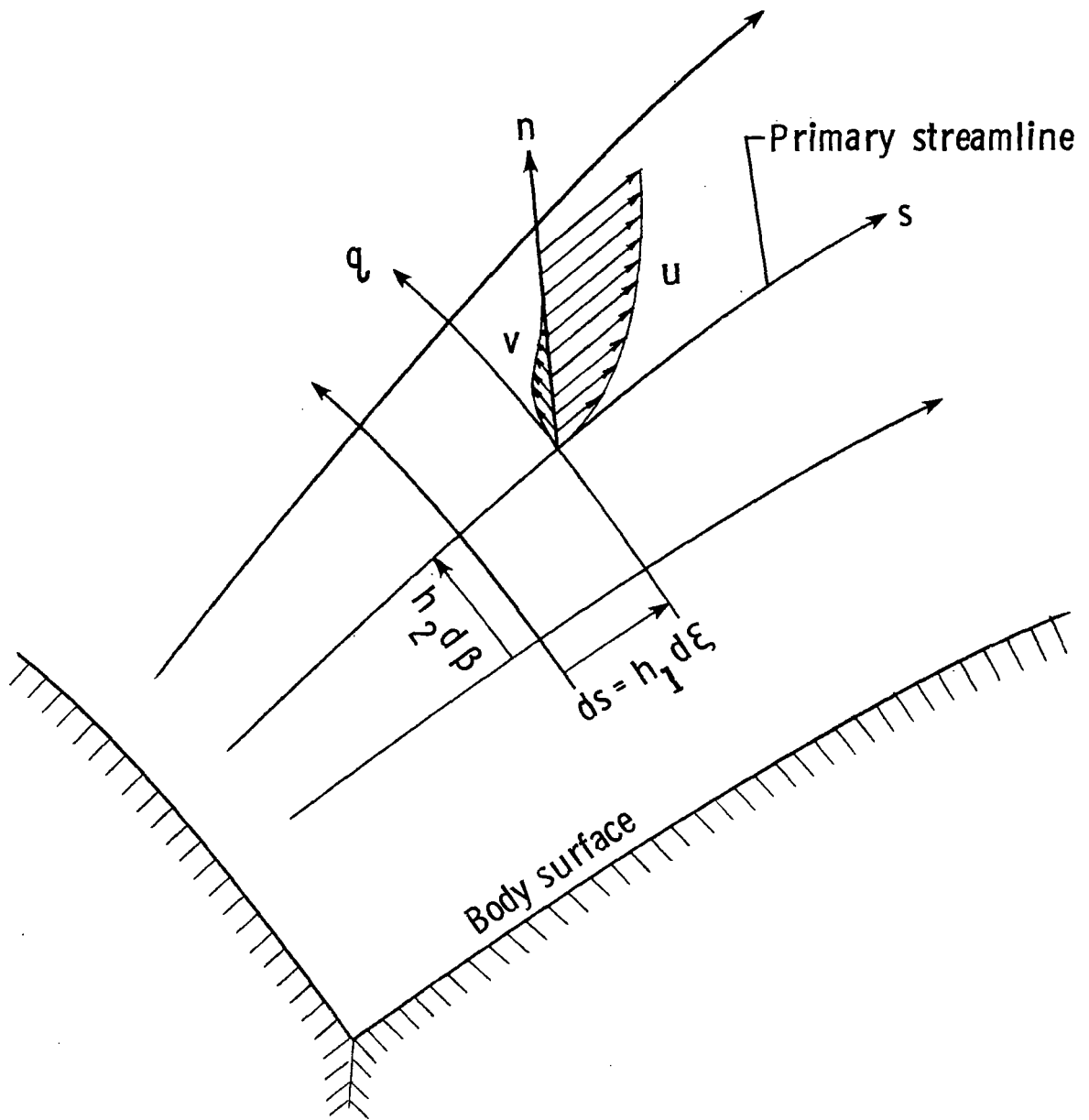
Figure 1.- Typical surface streamlines and boundary-layer velocity profile.
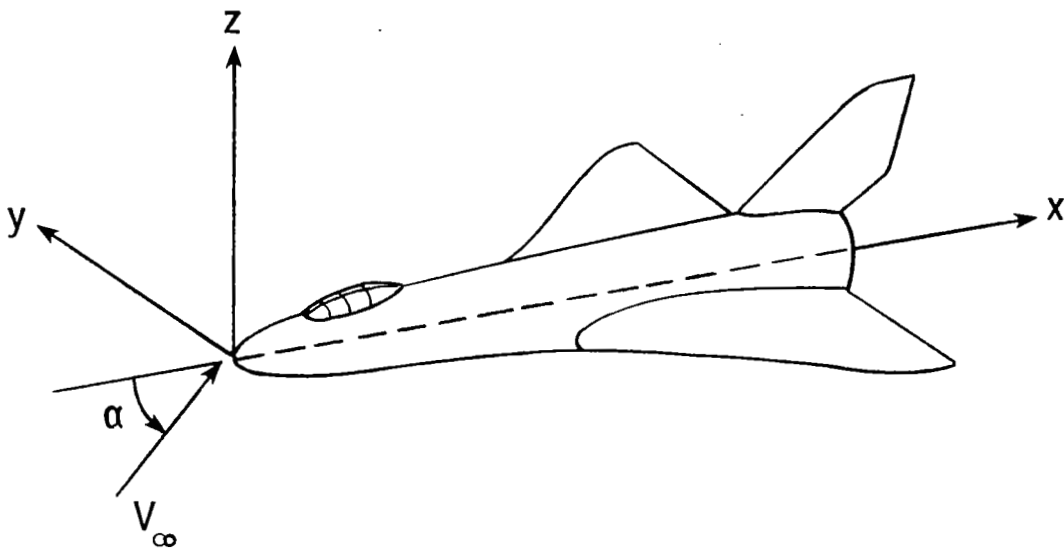
Figure 2.- Typical advanced reentry vehicle.
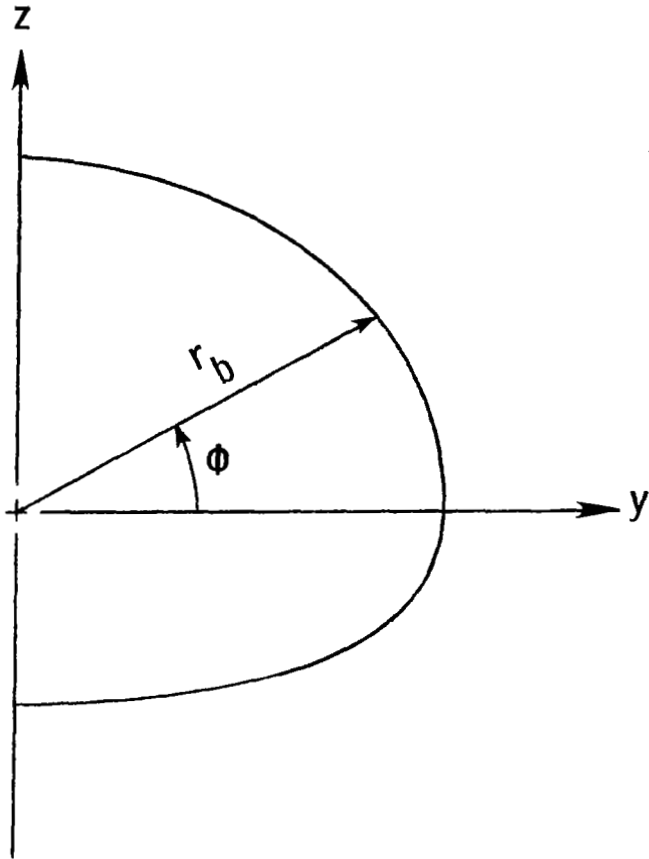
Figure 3.- Cylindrical coordinate system.
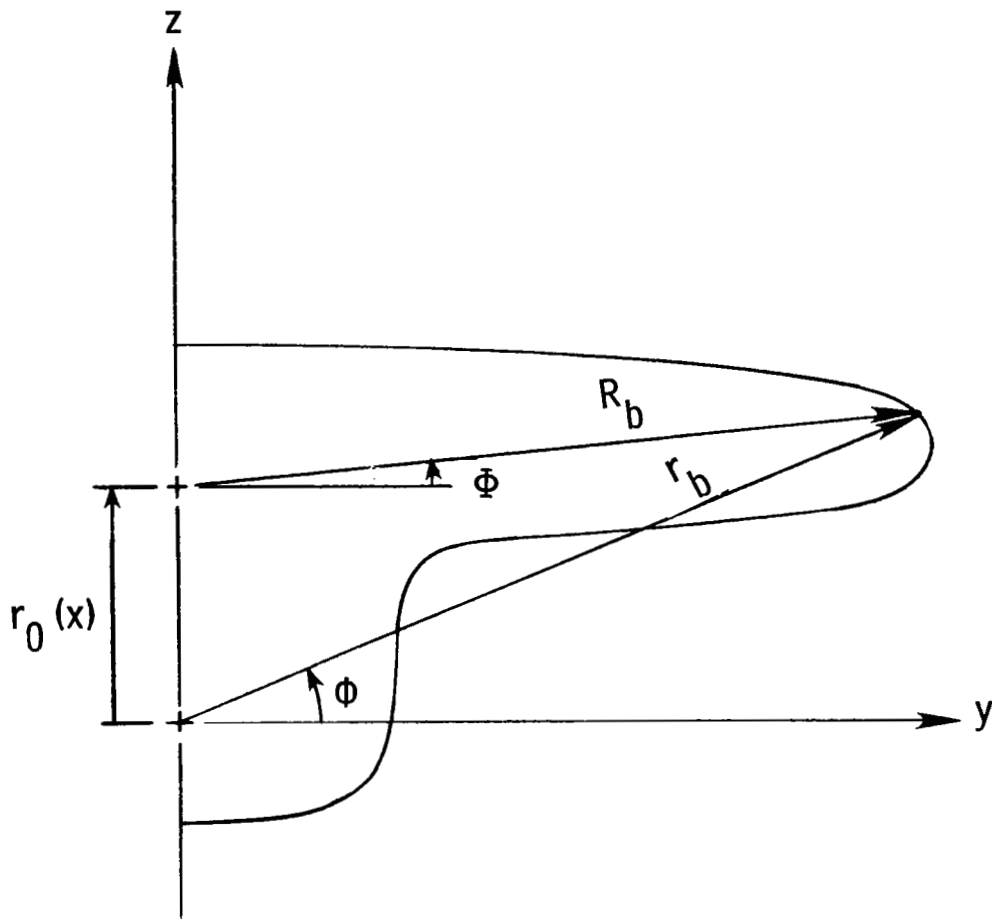
Figure 4.- Local polar coordinate system.
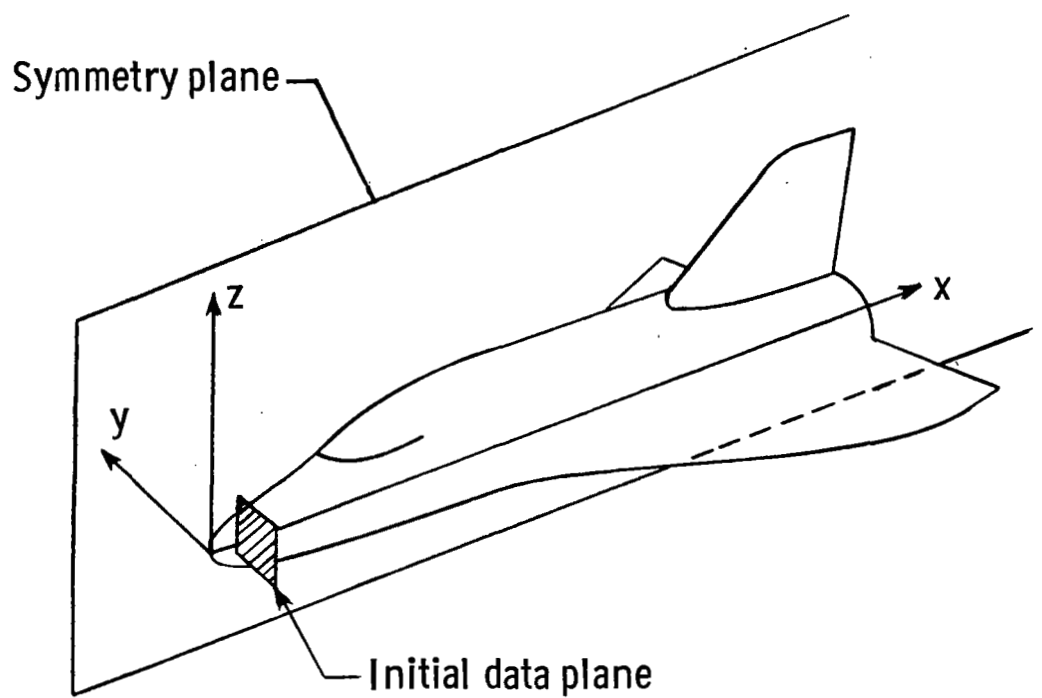
Figure 5.- Illustration of flow field calculation procedure.
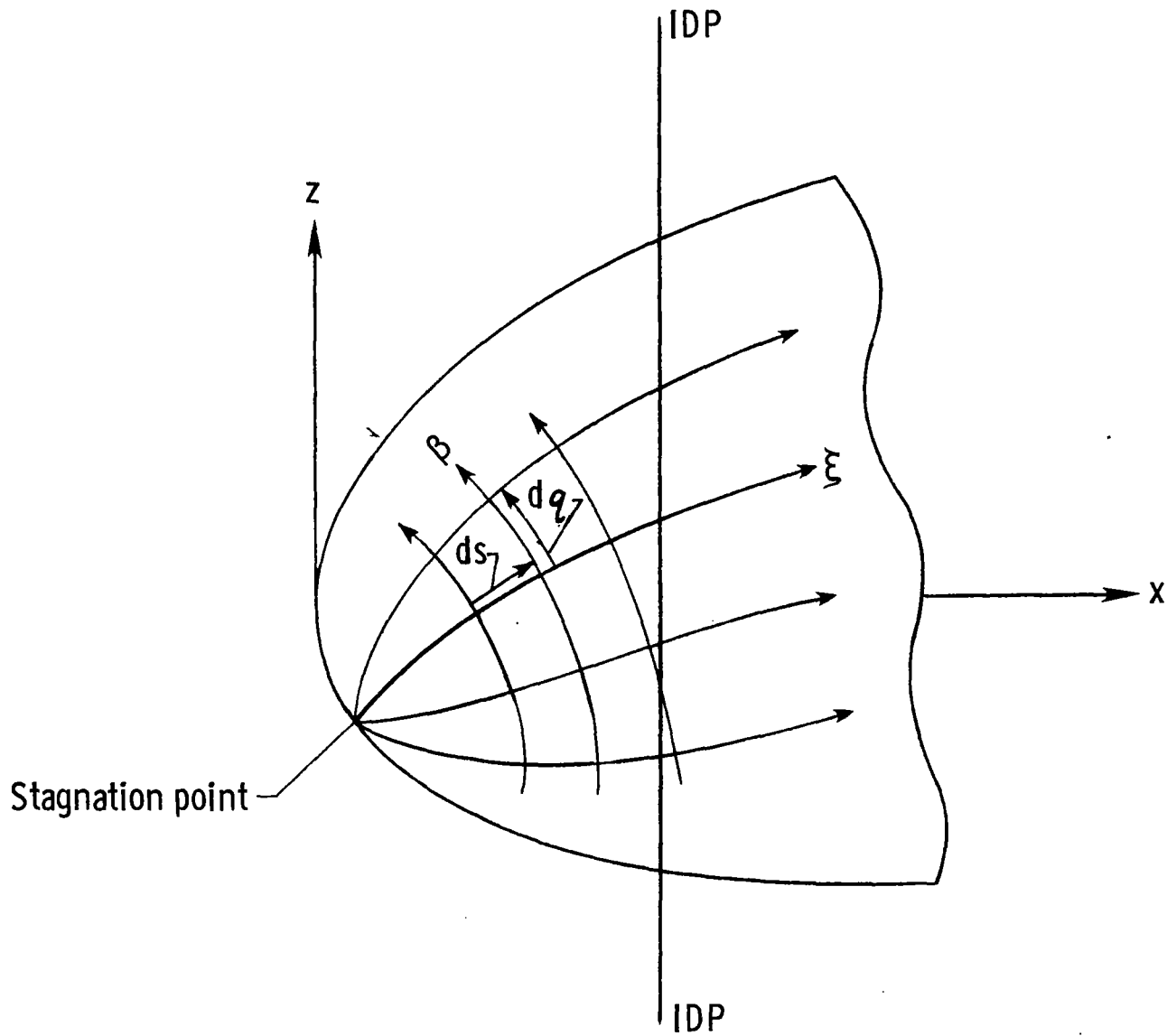
Figure 6.- Streamline pattern of nose of general three-dimensional vehicle.
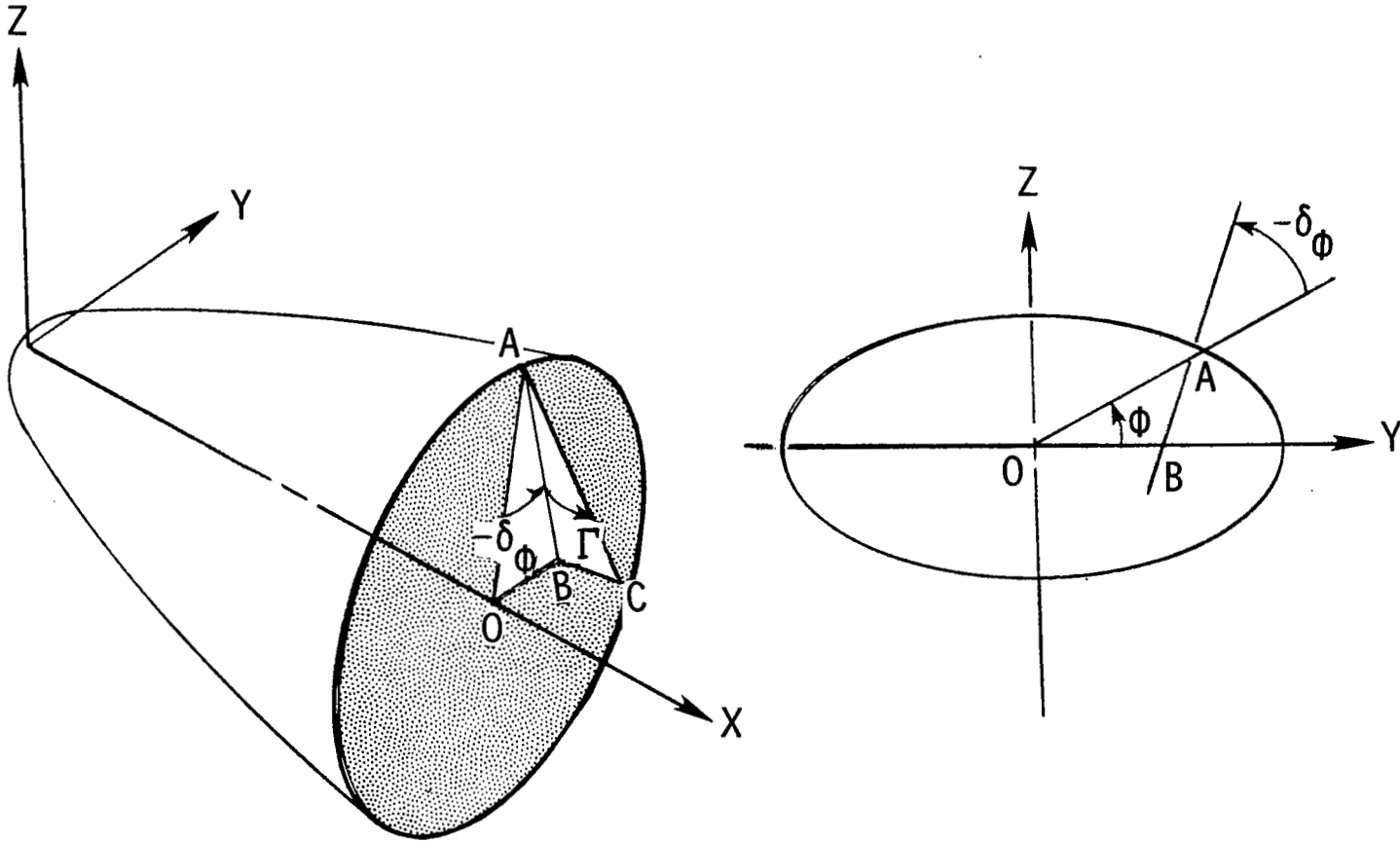
$$\overline{OA} = r_b$$

$\overline{AC}$ is normal to body at A

$\overline{AB}$ is projection of $\overline{AC}$ on cross-sectional plane

Figure 7.- Definition of body-geometry angles δ_ϕ and Γ.
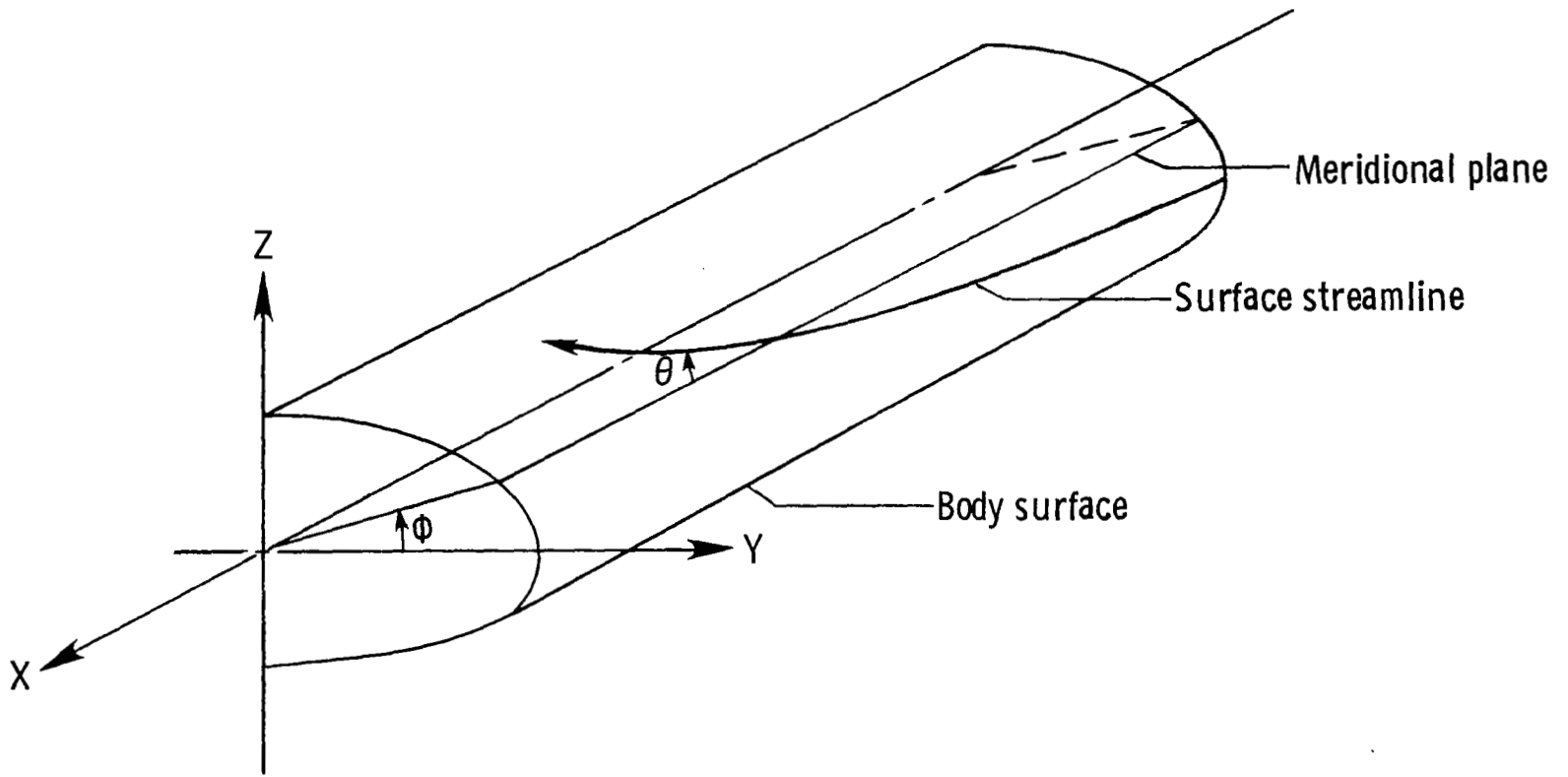
Figure 8.- Definition of velocity-direction angle θ.
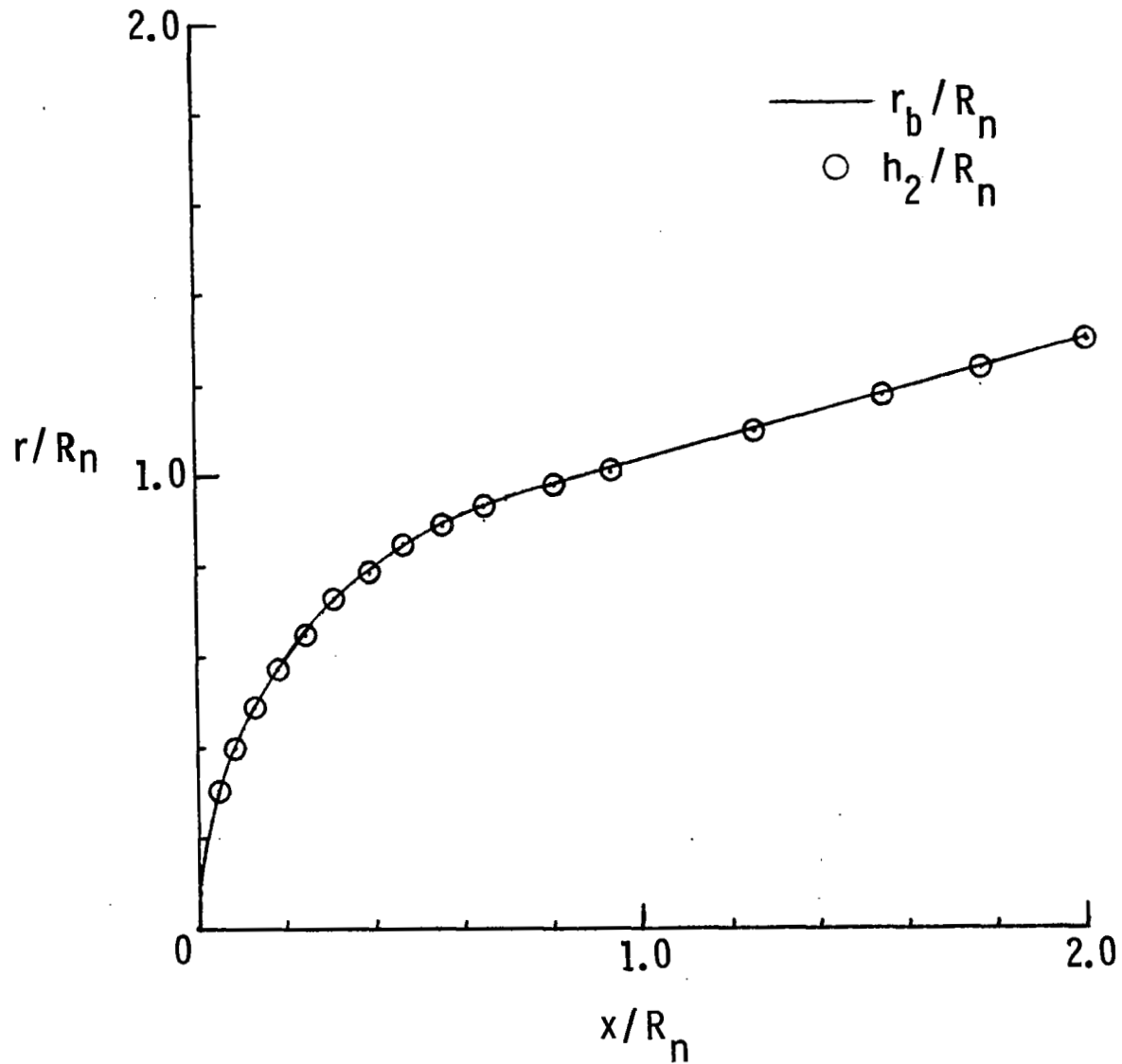
(a) $x/R_n \leqq 2$.

Figure 9.- Comparison of metric coefficients with body cross-sectional radius
for spherically blunted 15° half-angle cone. $\alpha = 0°$; $M_\infty = 10.6$; $\gamma = 1.4$.
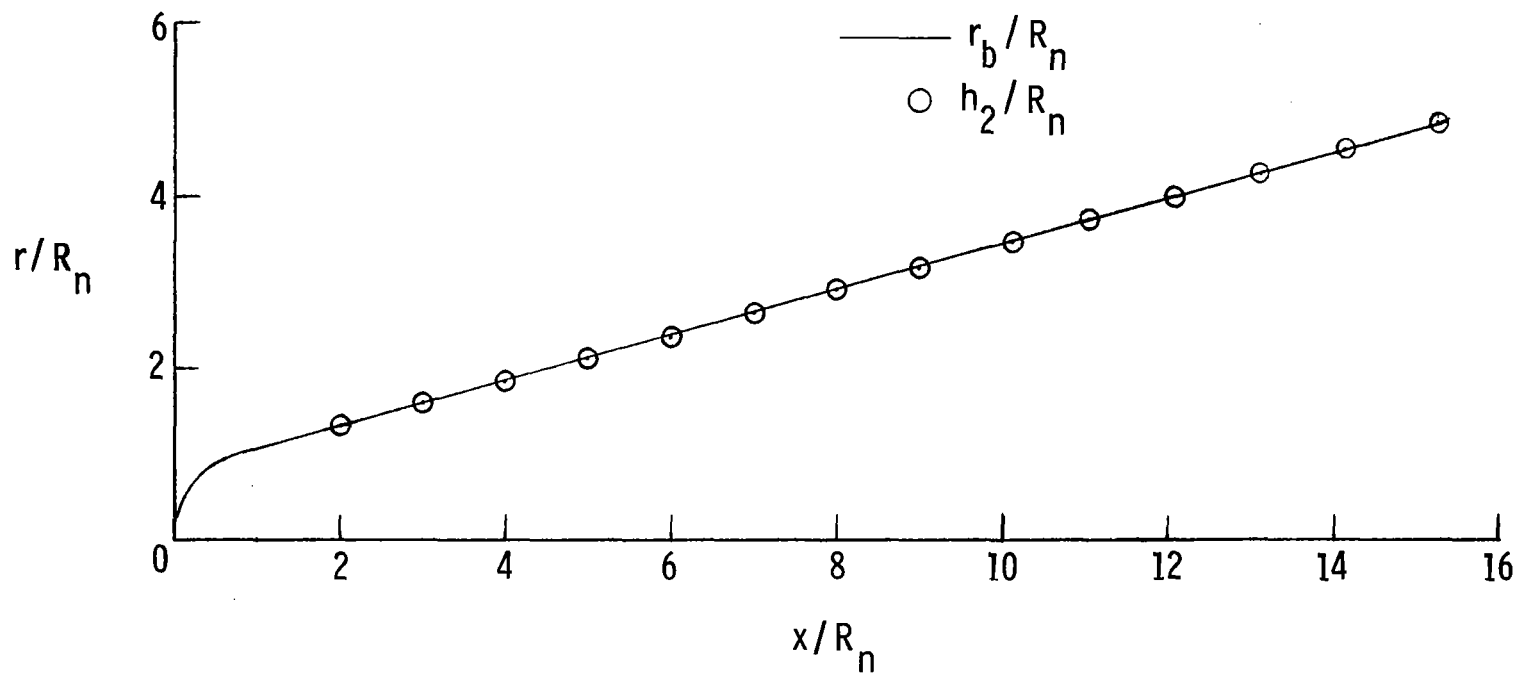
(b) $x/R_n \geq 2$.

Figure 9.- Concluded.
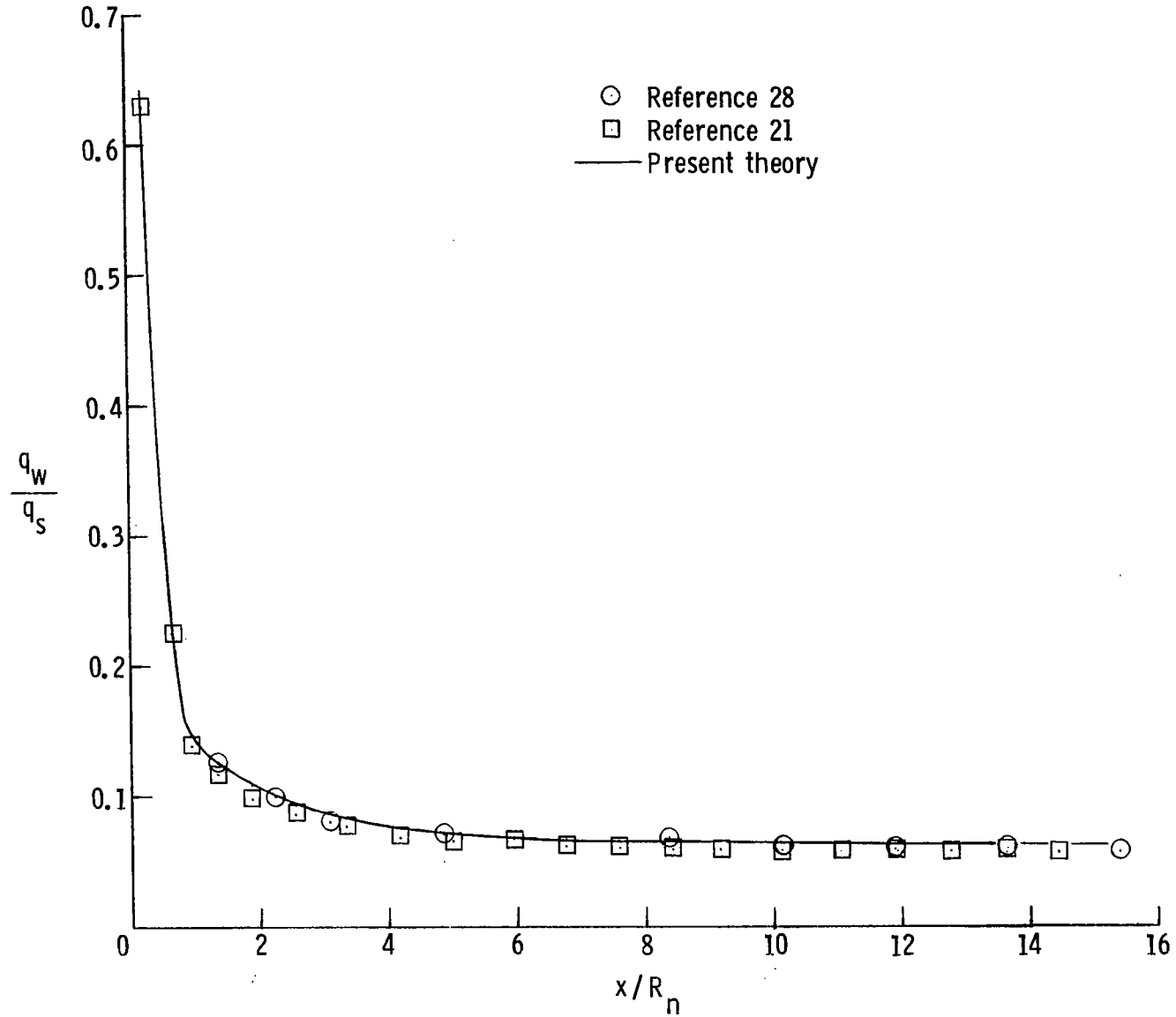
Figure 10.- Axial distribution of heating rate on a spherically blunted 15° half-angle cone at $\alpha = 0°$. $M_\infty = 10.6$; $\gamma = 1.4$; $N_{Re,\infty} = 1.31 \times 10^6$ per meter; $\zeta_w = 0.27$; $R_n = 0.95$ cm; $q_S = 224.32$ kW/m²-s.
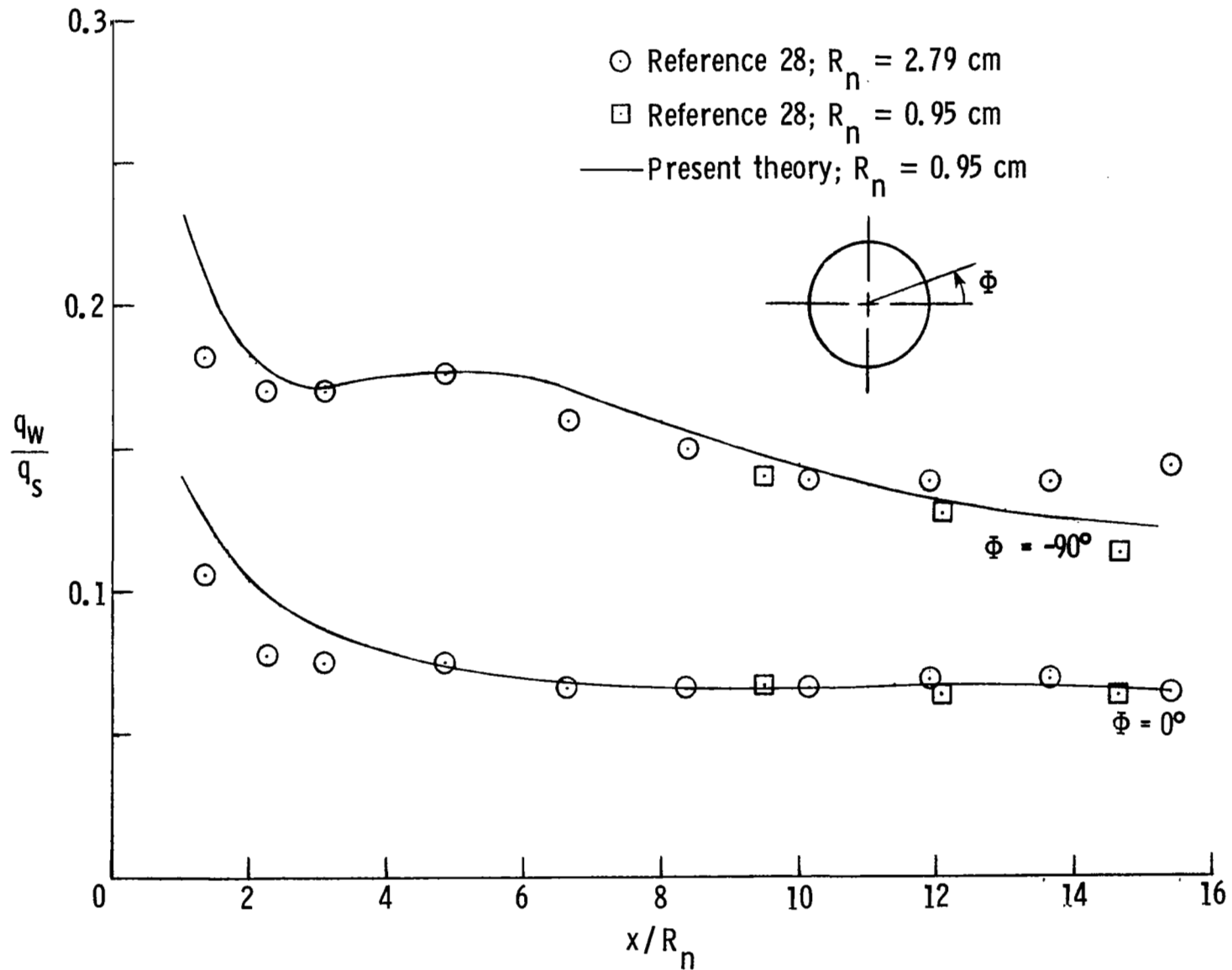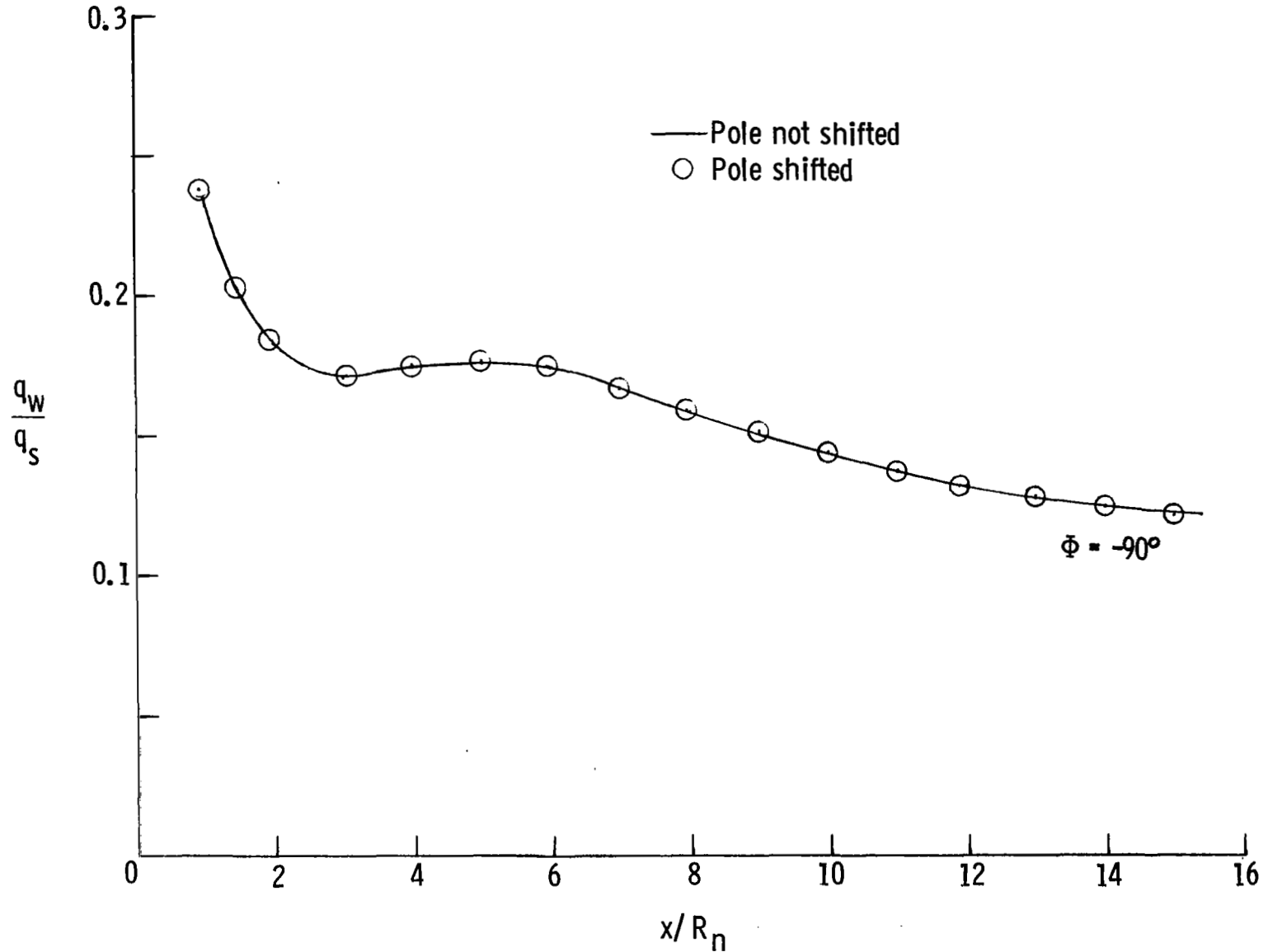
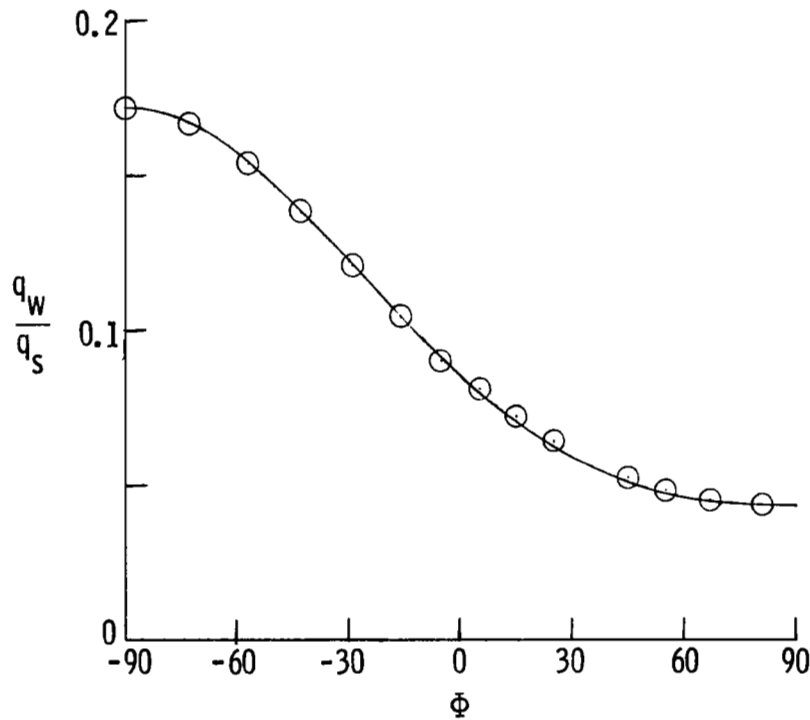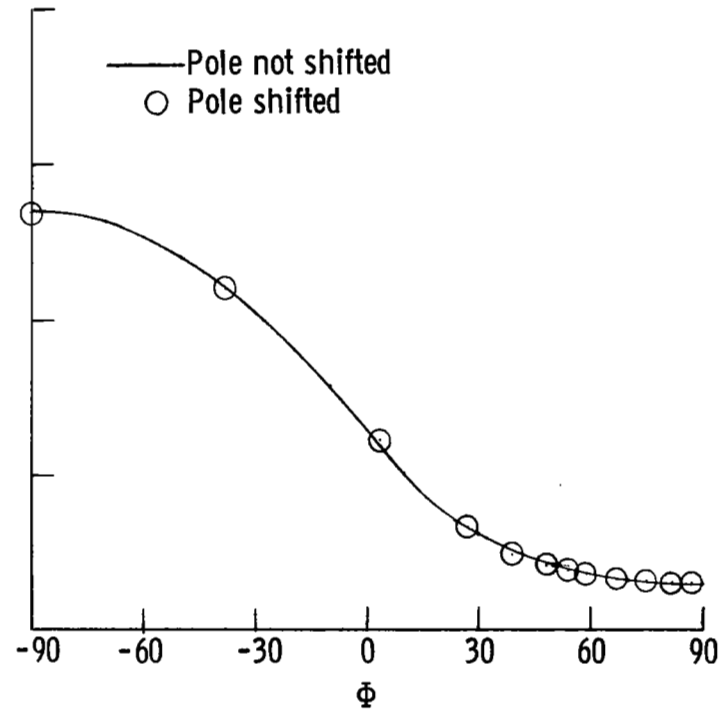Figure 11.- Axial distribution of heating rate on a spherically blunted 15° half-angle cone at $\alpha = 10°$. $M_\infty = 10.6$; $\gamma = 1.4$; $N_{Re,\infty} = 1.31 \times 10^6$ per meter; $\zeta_w = 0.27$; $q_s = 224.32$ kW/m^2-s.

○ Reference 28; R_n = 2.79 cm

□ Reference 28; R_n = 0.95 cm

—— Present theory; R_n = 0.95 cm

(a) x/R_n = 3.1.

(b) x/R_n = 12.0.
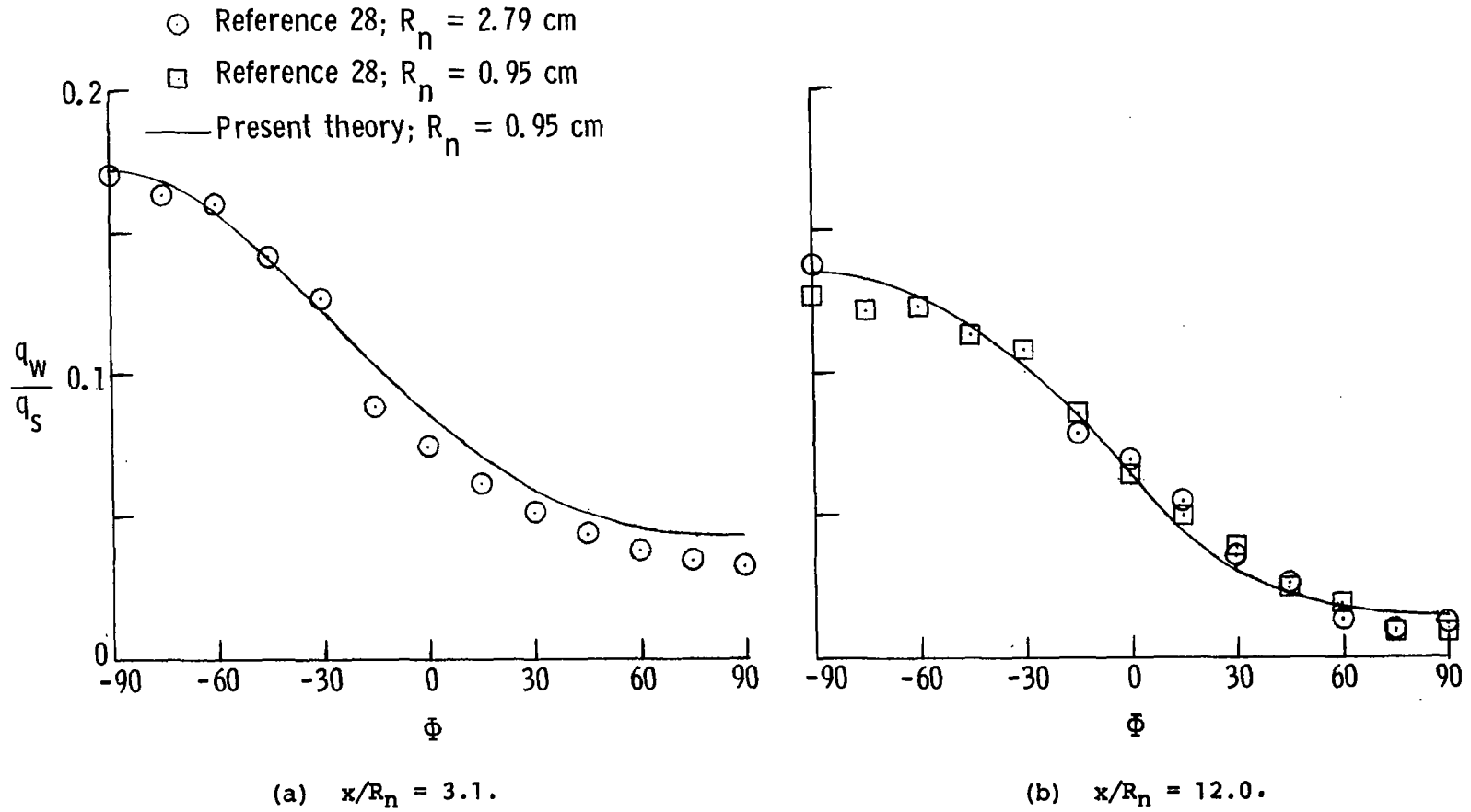
Figure 12.- Circumferential distribution of heating rate on a spherically blunted 15° half-angle cone at $\alpha = 10^O$. $M_\infty = 10.6$; $\gamma = 1.4$; $N_{Re,\infty} = 1.31 \times 10^6$ per meter; $\zeta_w = 0.27$; $q_S = 224.32$ kW/m^2-s.
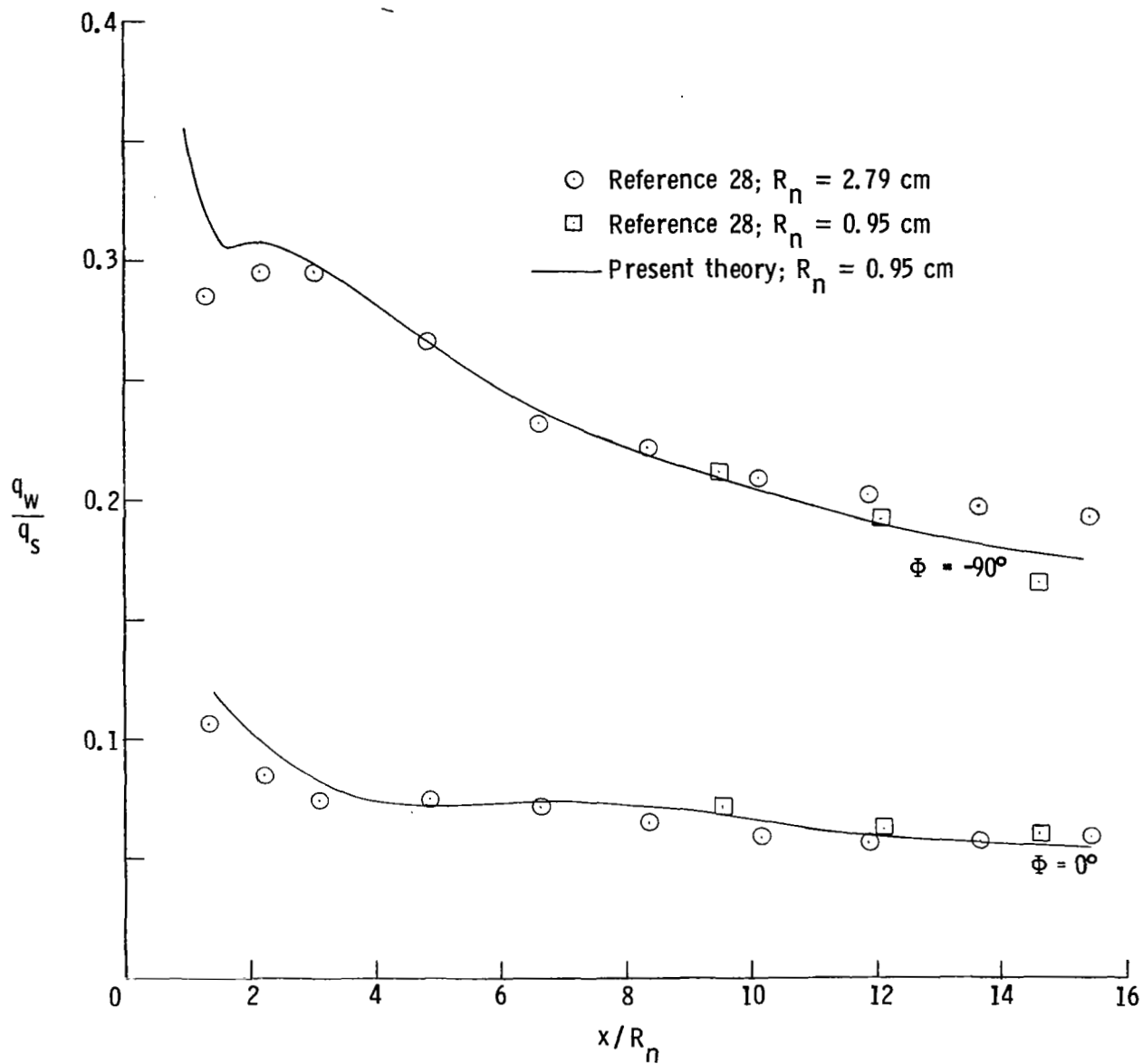
Figure 13.- Axial distribution of heating rate on a spherically blunted $15°$ half-angle cone at $\alpha = 20°$. $M_\infty = 10.6$; $\gamma = 1.4$; $N_{Re,\infty} = 1.31 \times 10^6$ per meter; $\zeta_w = 0.27$; $q_S = 224.32$ kW/m^2-s.
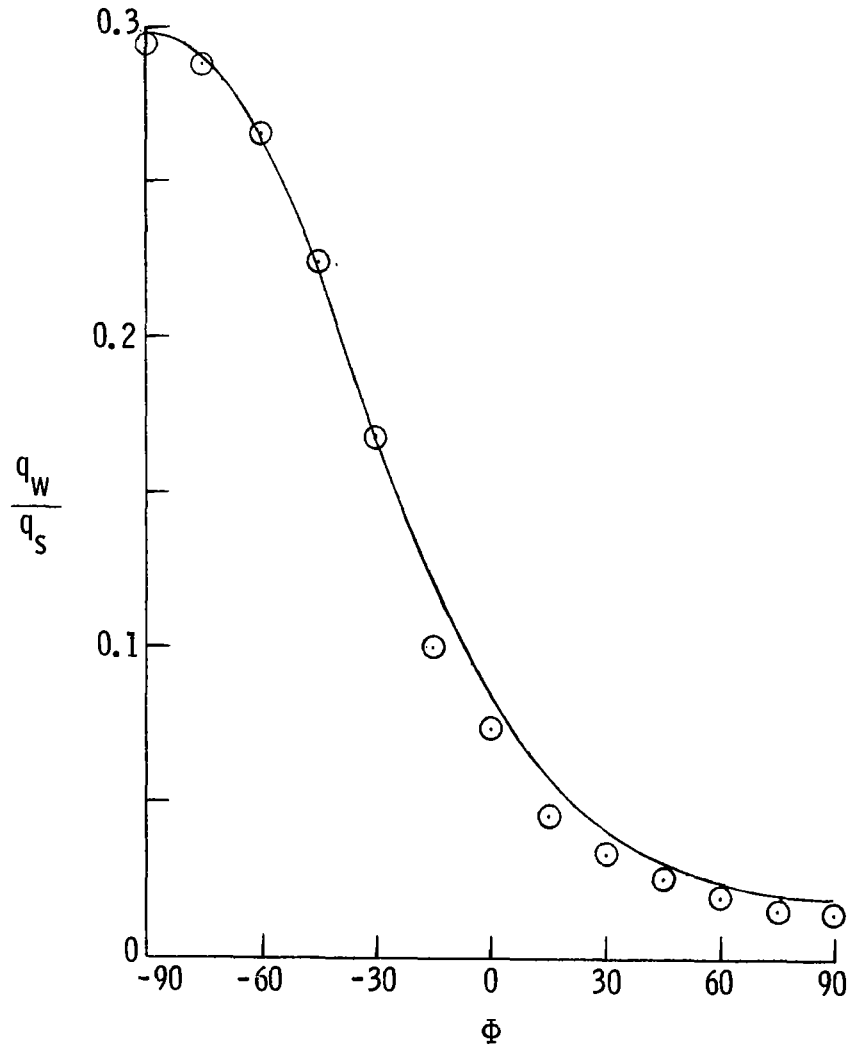
(a) x/R_n = 3.1.
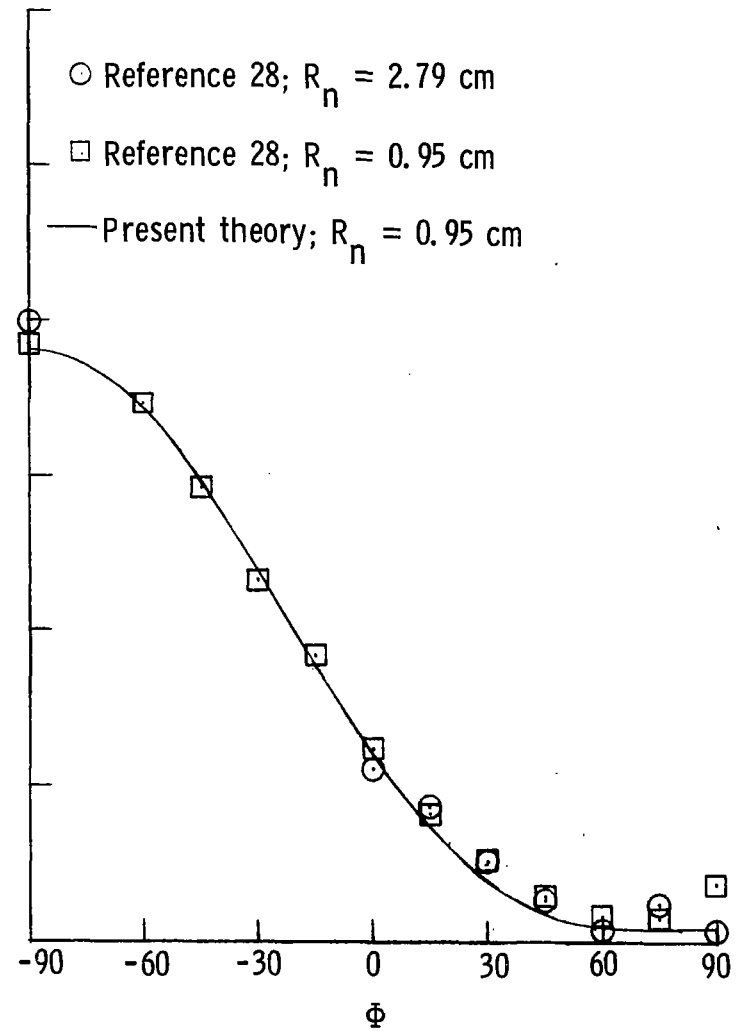
(b) x/R_n = 12.0.

Figure 14.- Circumferential distribution of heating rate on a spherically blunted 15° half-angle cone at α = 20°. M_∞ = 10.6; γ = 1.4; $N_{Re,\infty}$ = 1.31 × 10^6 per meter; ζ_w = 0.27; q_s = 224.32 kW/m^2-s.
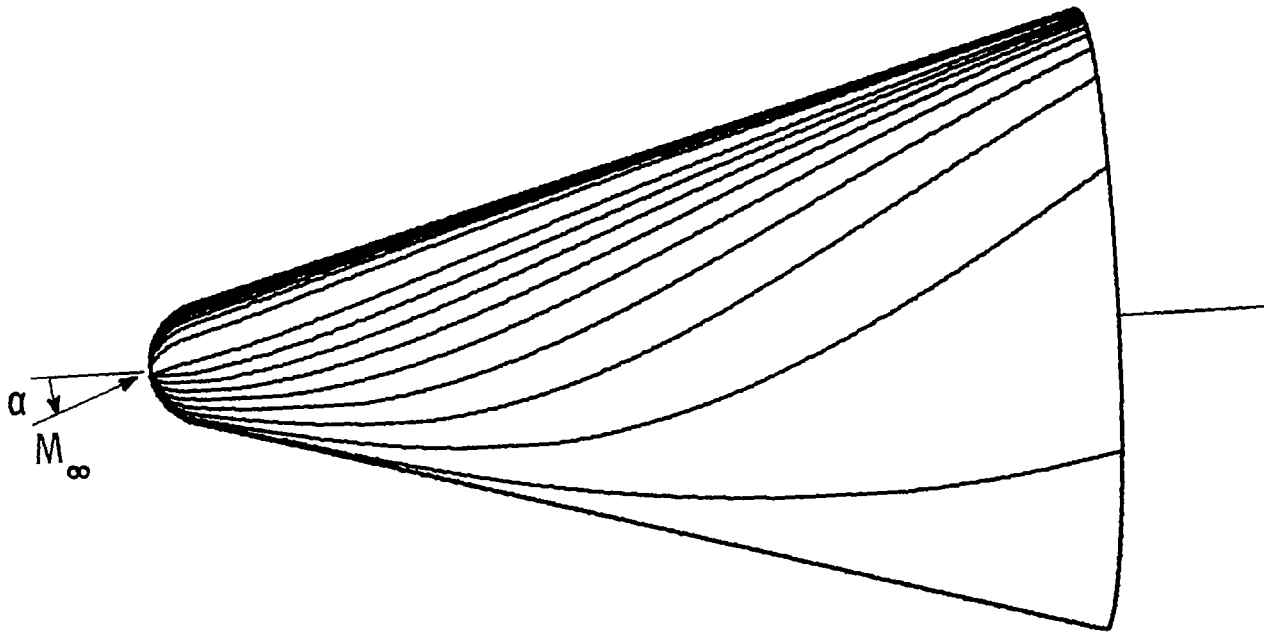
Figure 15.- Side view of inviscid surface streamline pattern on a spherically blunted 15° half-angle cone at $\alpha = 20°$. $M_\infty = 10.6$; $\gamma = 1.4$.
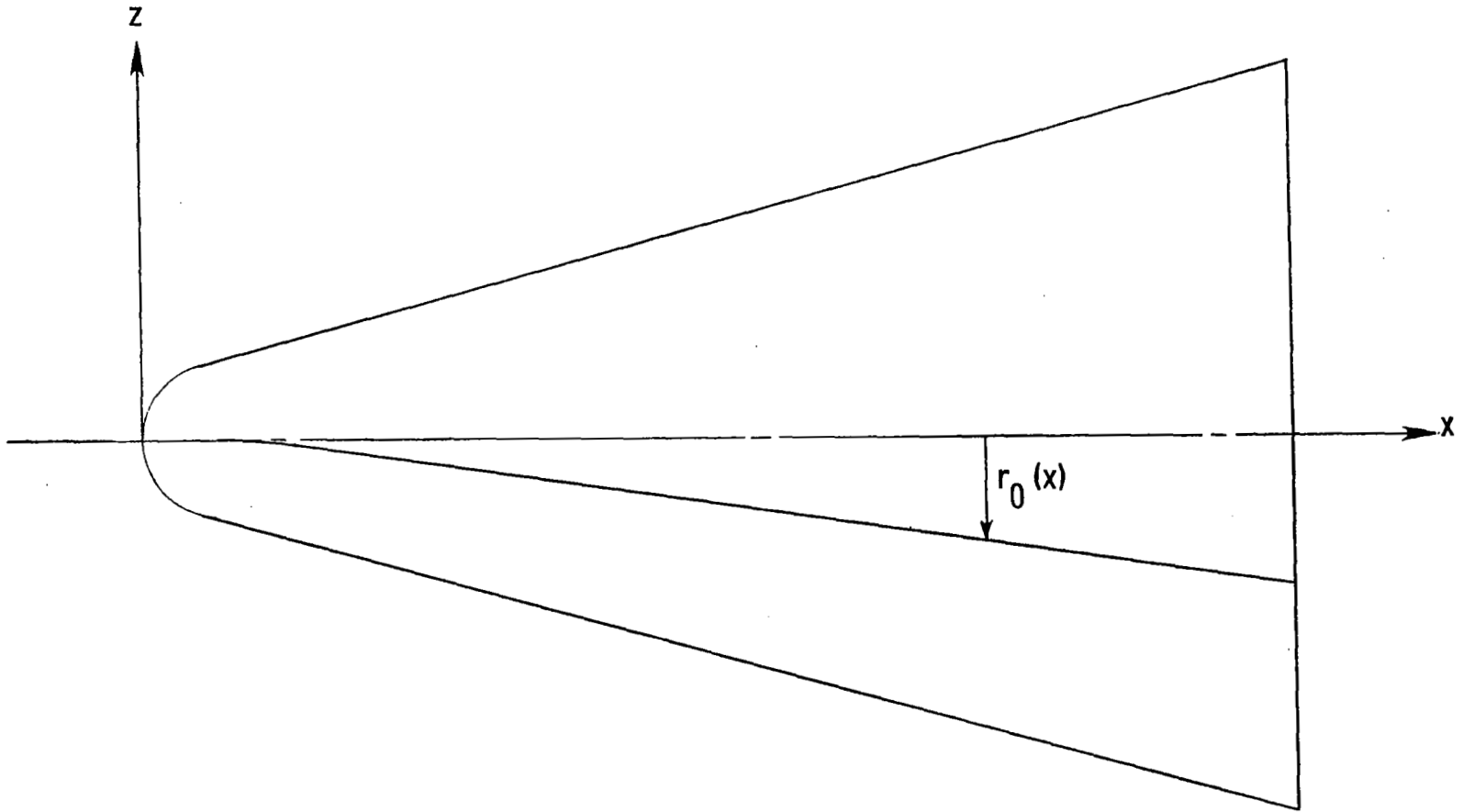
Figure 16.- Geometry of shifted pole for spherically blunted 15° half-angle cone.
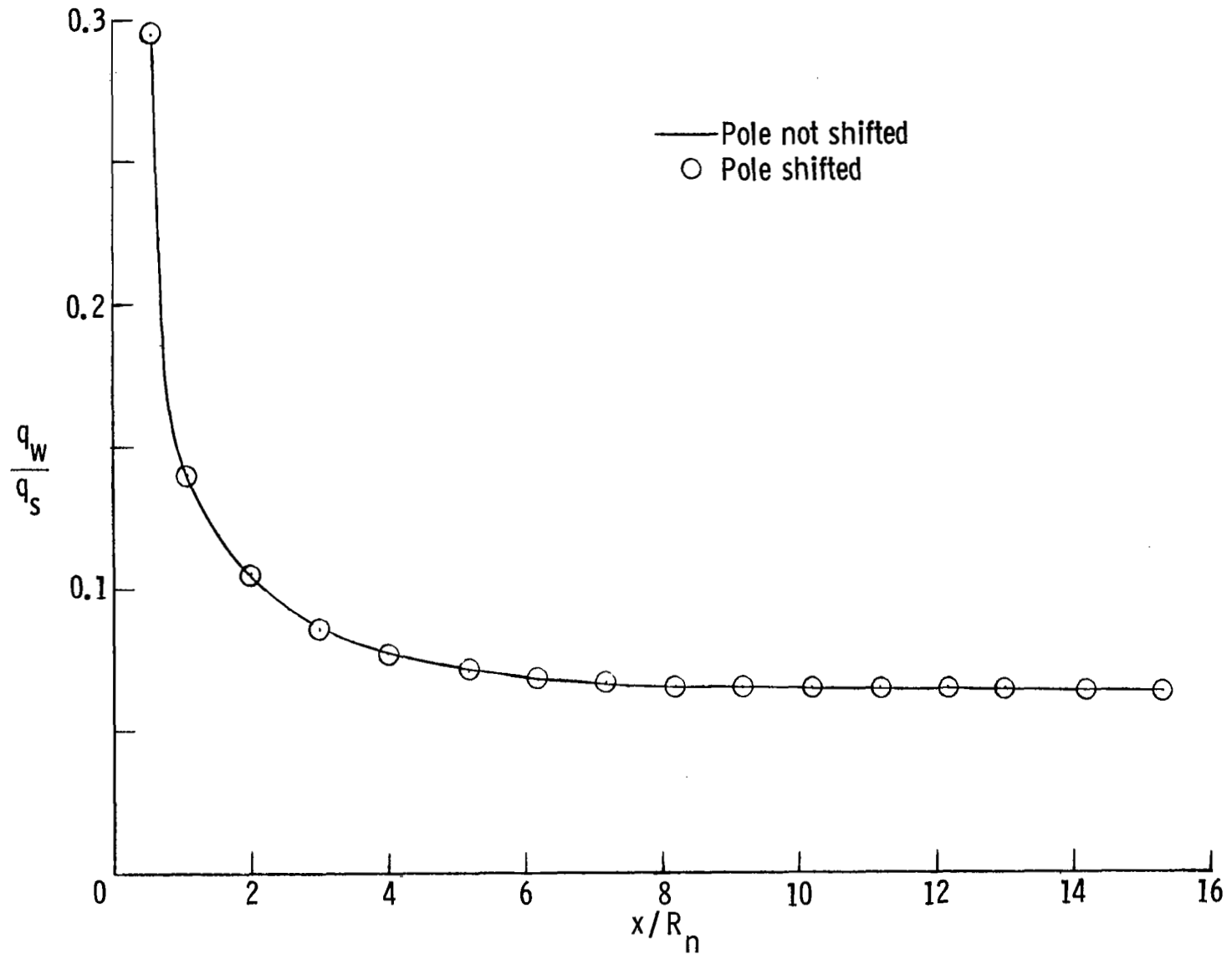
Figure 17.- Comparison of axial heat-transfer calculations on a spherically blunted 15° half-angle cone with shifted and unshifted poles at $\alpha = 0^{\circ}$. $M_{\infty} = 10.6$; $\gamma = 1.4$; $N_{Re,\infty} = 1.31 \times 10^{6}$ per meter; $\zeta_w = 0.27$; $R_n = 0.95$ cm; $q_s = 224.32$ kW/m^2-s.

Figure 18.- Comparison of axial heat-transfer calculations on a spherically blunted 15° half-angle cone with shifted and unshifted poles at $\alpha = 10°$. $M_\infty = 10.6$; $\gamma = 1.4$; $N_{Re,\infty} = 1.31 \times 10^6$ per meter; $\zeta_w = 0.27$; $R_n = 0.95$ cm; $q_S = 224.32$ kW/m^2-s.

(a) $x/R_n = 3.1.$ (b) $x/R_n = 12.0.$

Figure 19.- Comparison of circumferential heat-transfer calculations on a spherically blunted 15° half-angle cone with shifted and unshifted poles at $\alpha = 10^O$. $M_\infty = 10.6$; $\gamma = 1.4$; $N_{Re,\infty} = 1.31 \times 10^6$ per meter; $\zeta_w = 0.27$; $R_n = 0.95$ cm; $q_s = 224.32$ kW/m^2-s.
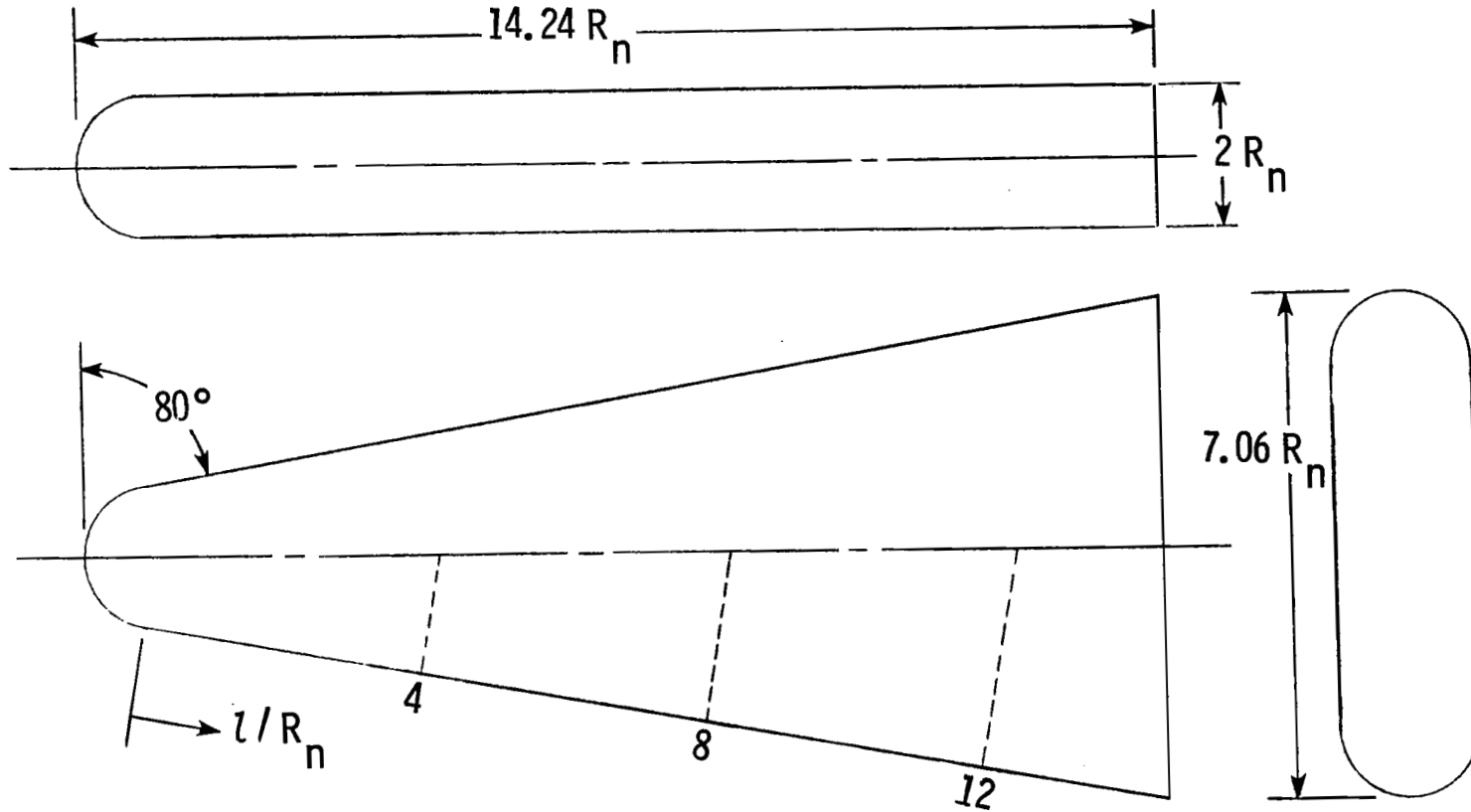
Figure 20.- 80° sweep slab delta wing. R_n = 1.27 cm.
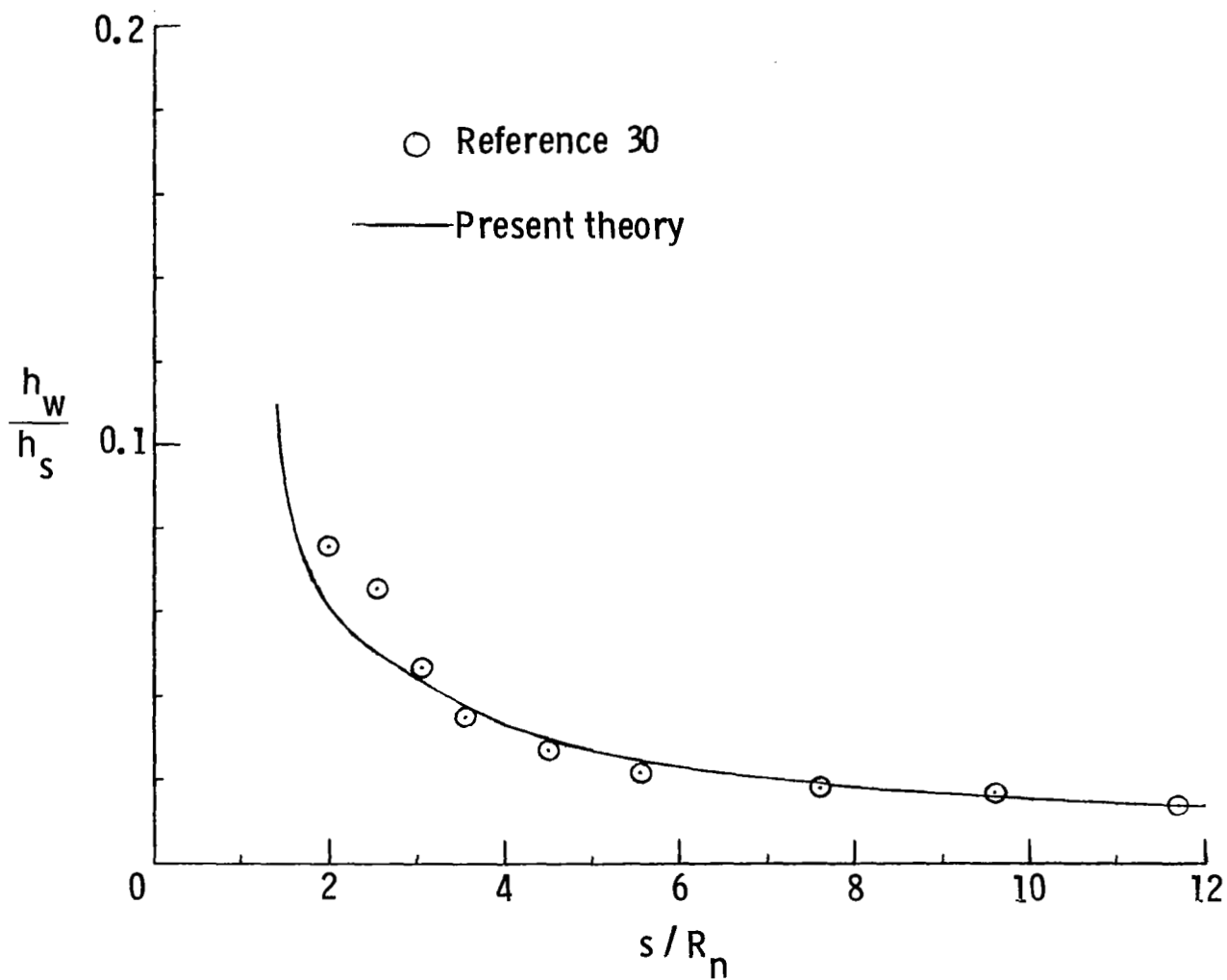
Figure 21.- Axial distribution of heat-transfer coefficient in windward symmetry plane of 80° sweep slab delta wing at $\alpha = 0°$. $M_\infty = 9.6$; $\gamma = 1.4$; $N_{Re,\infty} = 3.94 \times 10^6$ per meter; $\zeta_w = 0.33$; $R_n = 1.27$ cm; $h_S = 0.3796$ kW/m²-s-K.

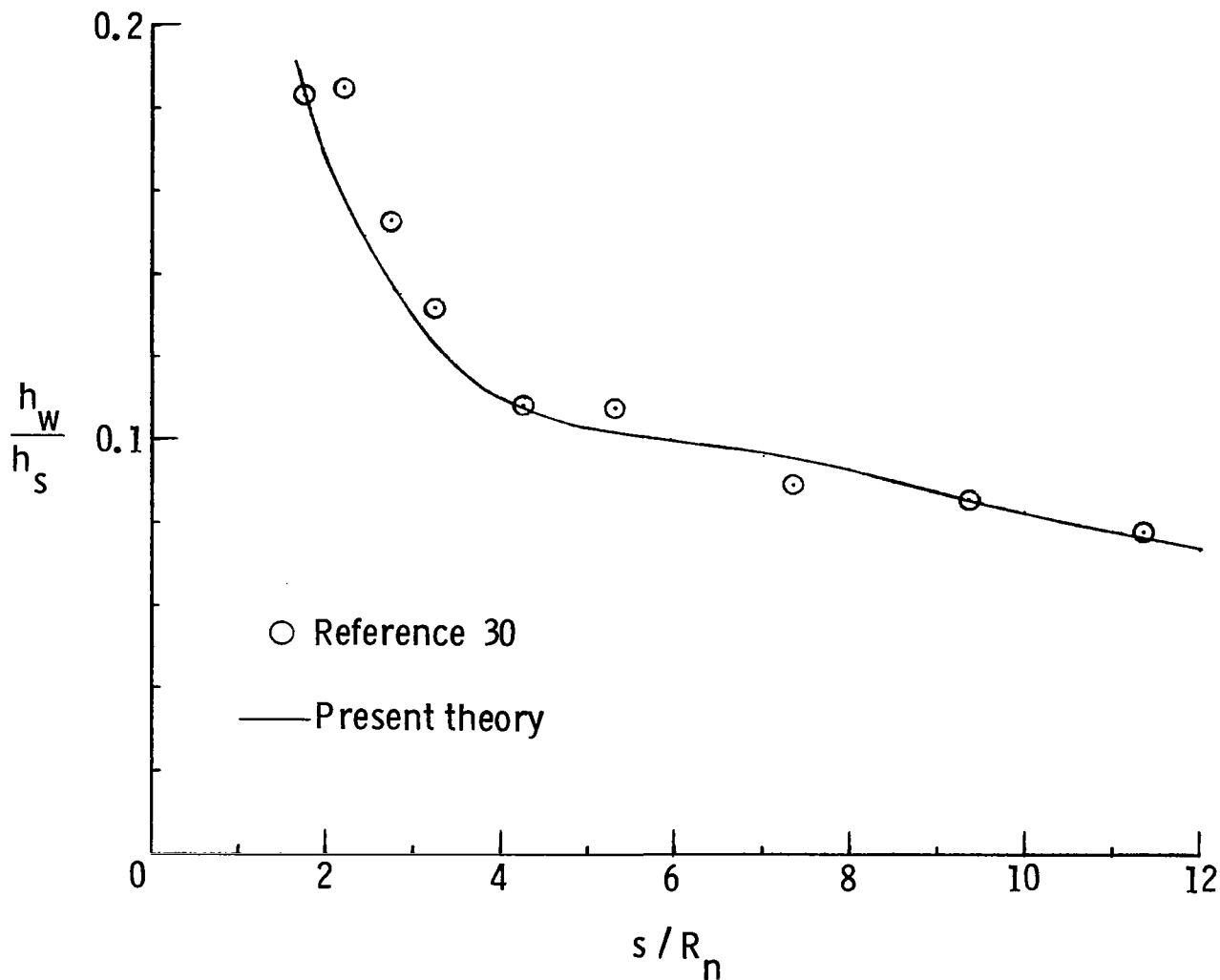(a) $l/R_n = 4.$ (b) $l/R_n = 8.$ (c) $l/R_n = 12.$

Figure 22.- Circumferential distribution of heat-transfer coefficient on a spherically blunted 80° sweep delta wing at $\alpha = 0^\circ$. $M_\infty = 9.6$; $\gamma = 1.4$; $N_{Re,\infty} = 3.94 \times 10^6$ per meter; $\zeta_w = 0.33$; $R_n = 1.27$ cm; $h_s = 0.3796$ kW/m²-s-K.
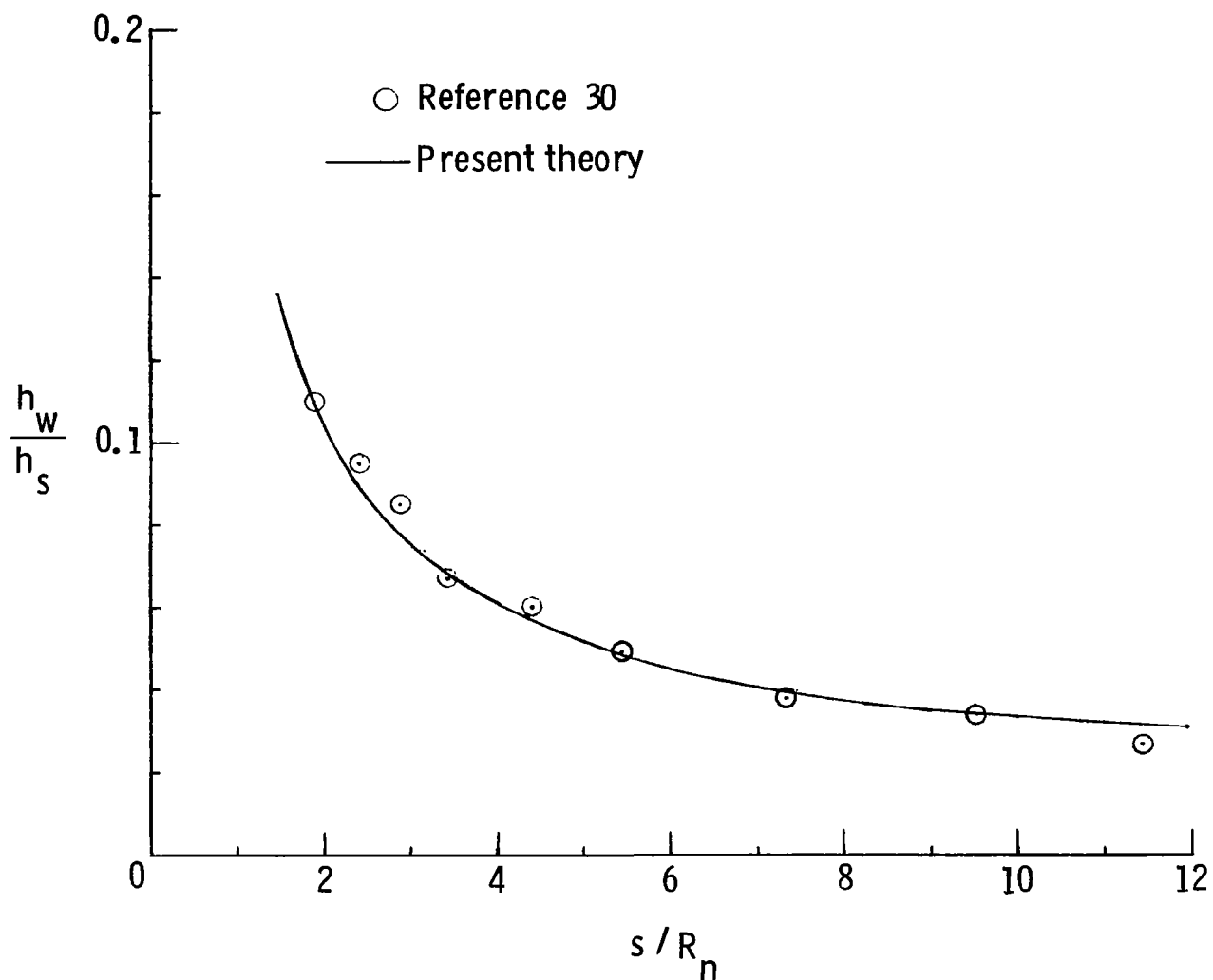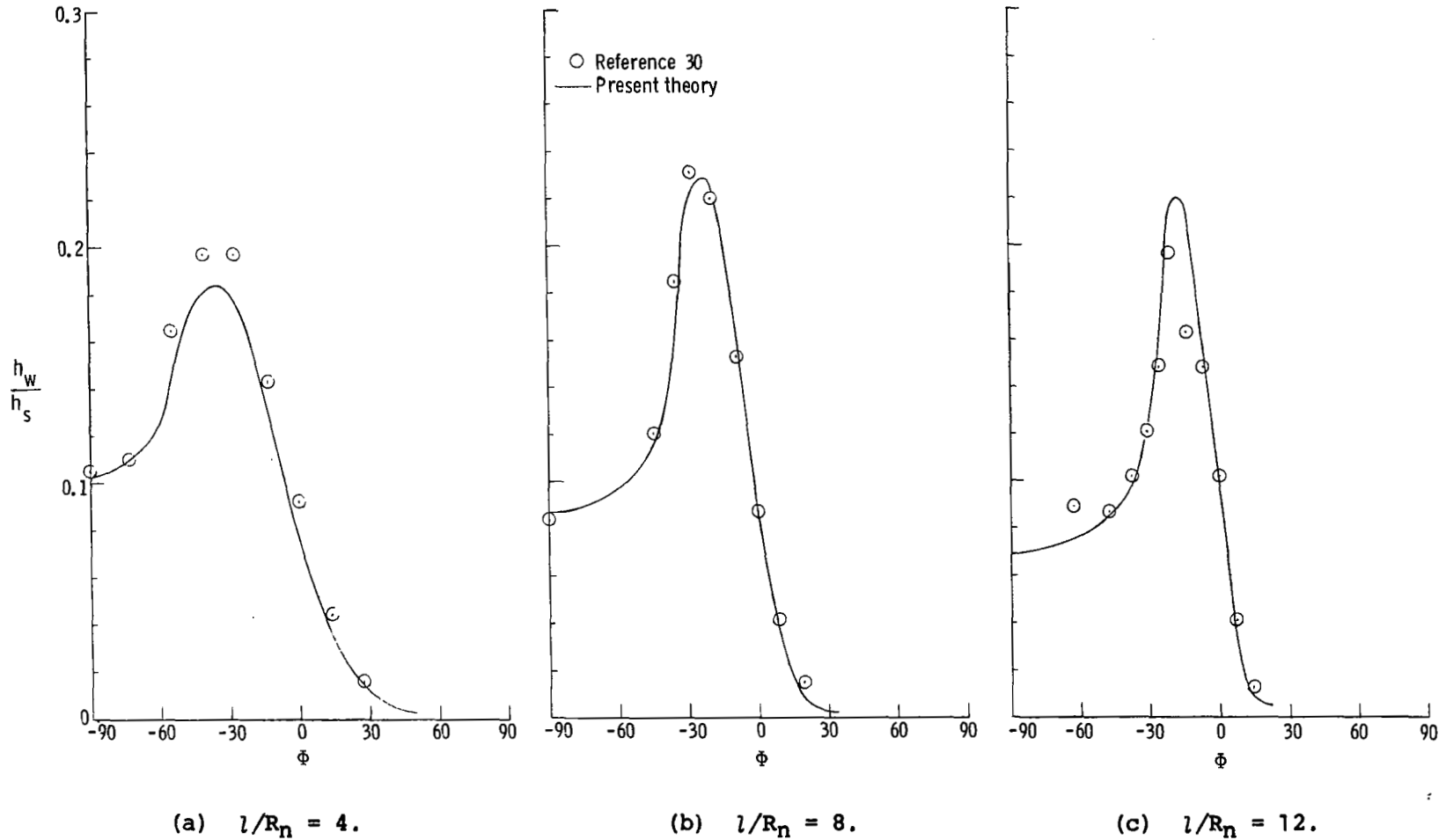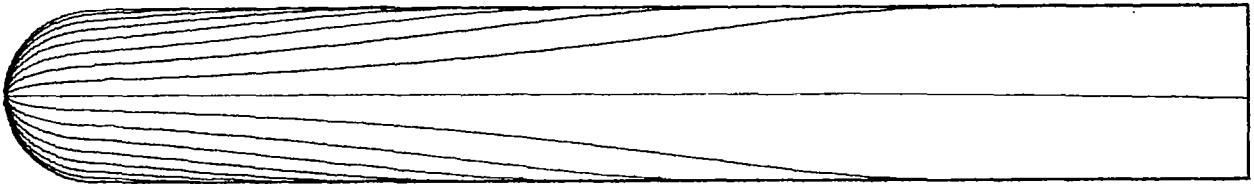
Figure 23.- Axial distribution of heat-transfer coefficient in windward symmetry plane of spherically blunted 80° sweep slab delta wing at $\alpha = 10°$. $M_\infty = 9.6$; $\gamma = 1.4$; $N_{Re,\infty} = 3.94 \times 10^6$ per meter; $\zeta_w = 0.33$; $R_n = 1.27$ cm; $h_s = 0.3796$ kW/m²-s-k.
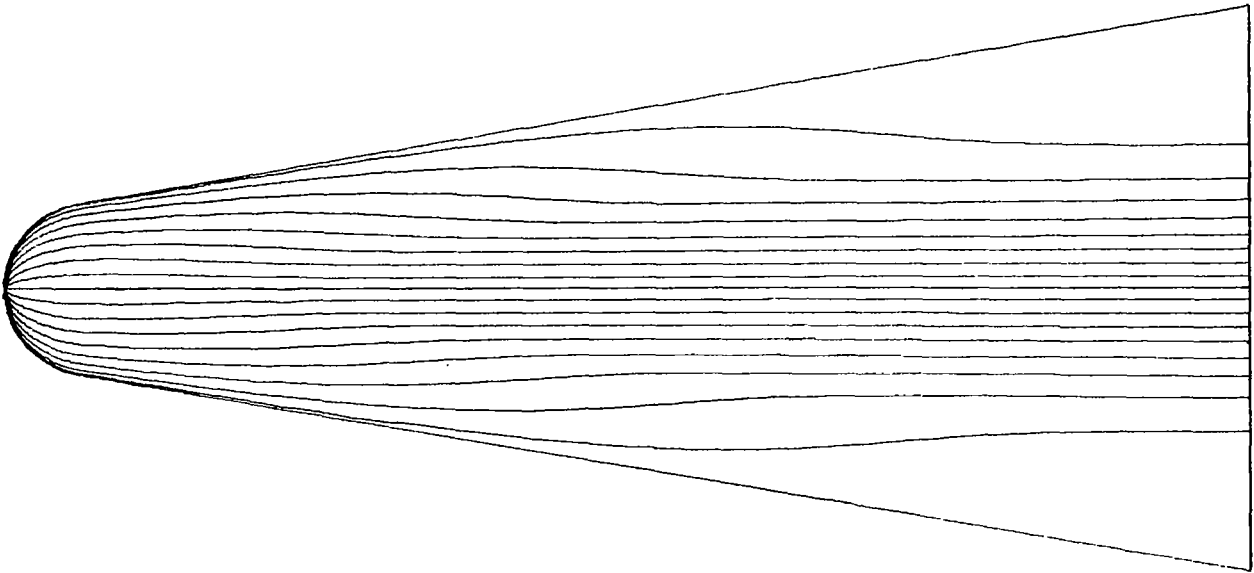
(a) $l/R_n = 4.$ (b) $l/R_n = 8.$ (c) $l/R_n = 12.$
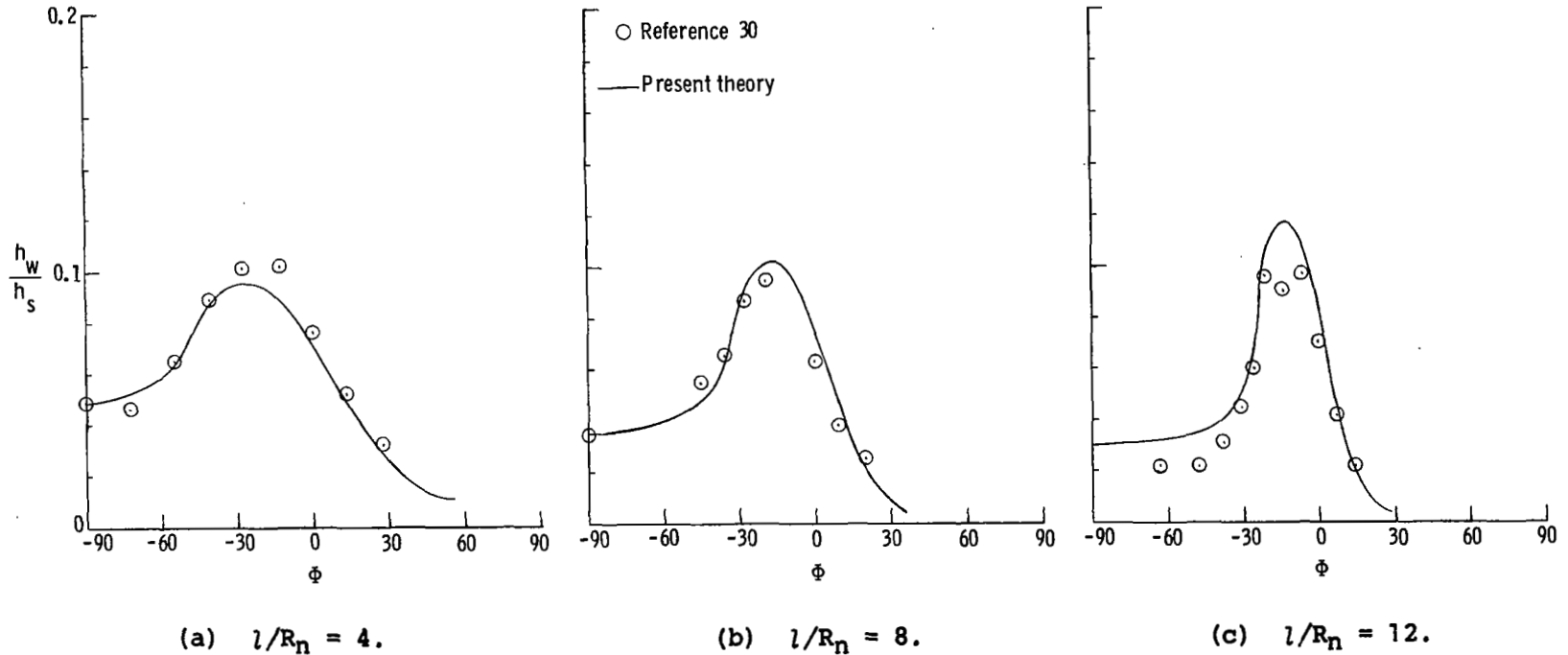
Figure 24.- Circumferential distribution of heat-transfer coefficient on spherically blunted 80° sweep slab delta wing at $\alpha = 10°$. $M_\infty = 9.6$; $\gamma = 1.4$; $N_{Re,\infty} = 3.94 \times 10^6$ per meter; $\zeta_w = 0.33$; $R_n = 1.27$ cm; $h_s = 0.3796$ kW/m^2-s-K.

Figure 25.- Axial distribution of heat-transfer coefficient in windward symmetry plane of a spherically blunted 80° sweep delta wing at α = 20°. M_∞ = 9.6; γ = 1.4; $N_{Re,\infty}$ = 3.94 × 10⁶ per meter; ζ_w = 0.33; R_n = 1.27 cm; h_S = 0.3796 kW/m²-s-K.

(a) $l/R_n = 4$.

(b) $l/R_n = 8$.

(c) $l/R_n = 12$.

Figure 26.- Circumferential distribution of heat-transfer coefficient on a spherically blunted 80° sweep slab delta wing at $\alpha = 20°$. $M_\infty = 9.6$; $\gamma = 1.4$; $N_{Re,\infty} = 3.94 \times 10^6$ per meter; $\zeta_w = 0.33$; $R_n = 1.27$ cm; $h_s = 0.3796$ kW/m²-s-K.

(a) Side view.

(b) Bottom view.

Figure 27.- Inviscid surface streamline pattern on a spherically blunted 80° sweep slab delta wing at $\alpha = 0°$. $M_\infty = 9.6$; $\gamma = 1.4$.

32.85 m

11.90 m

A

A

Section A-A
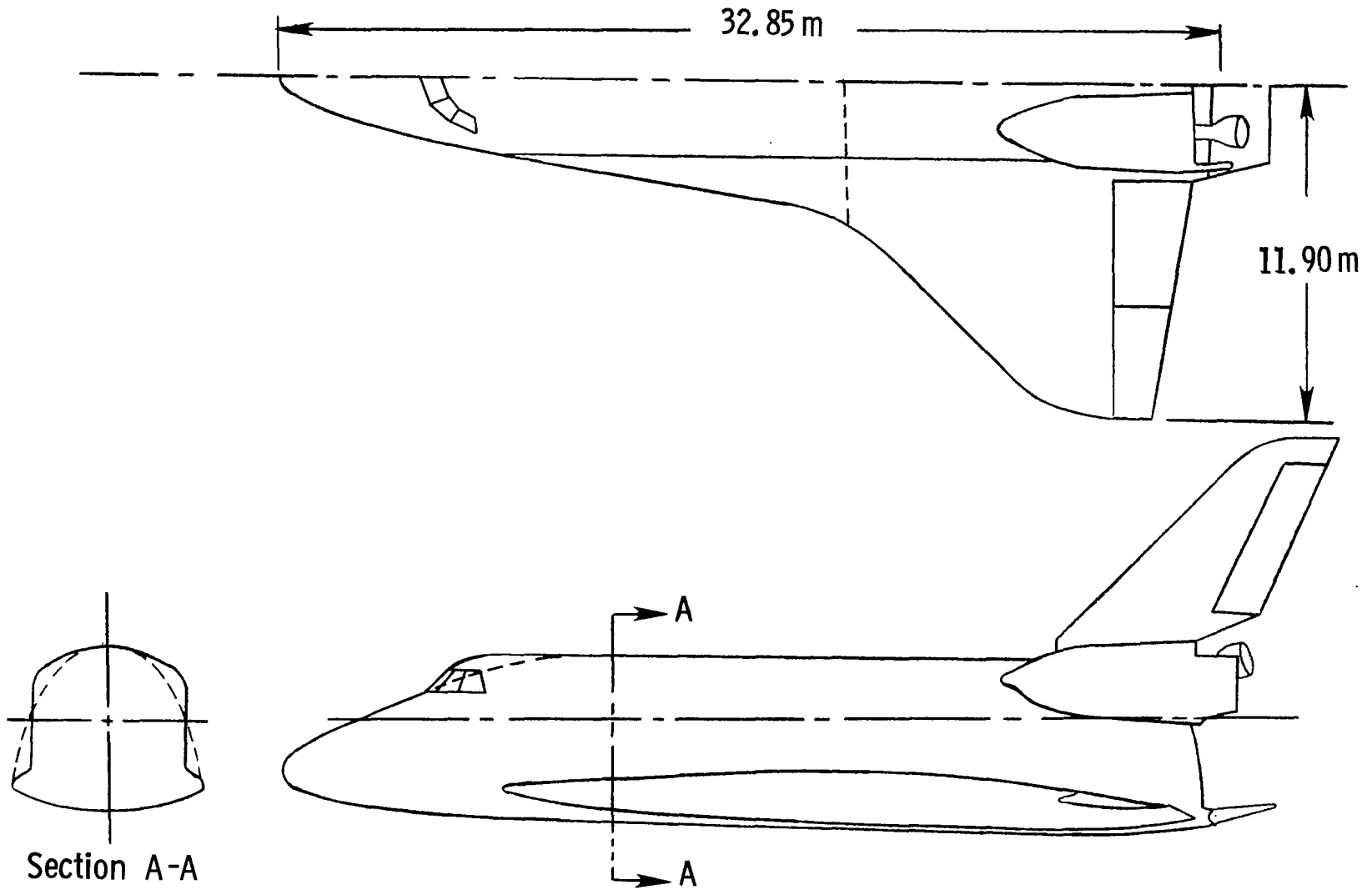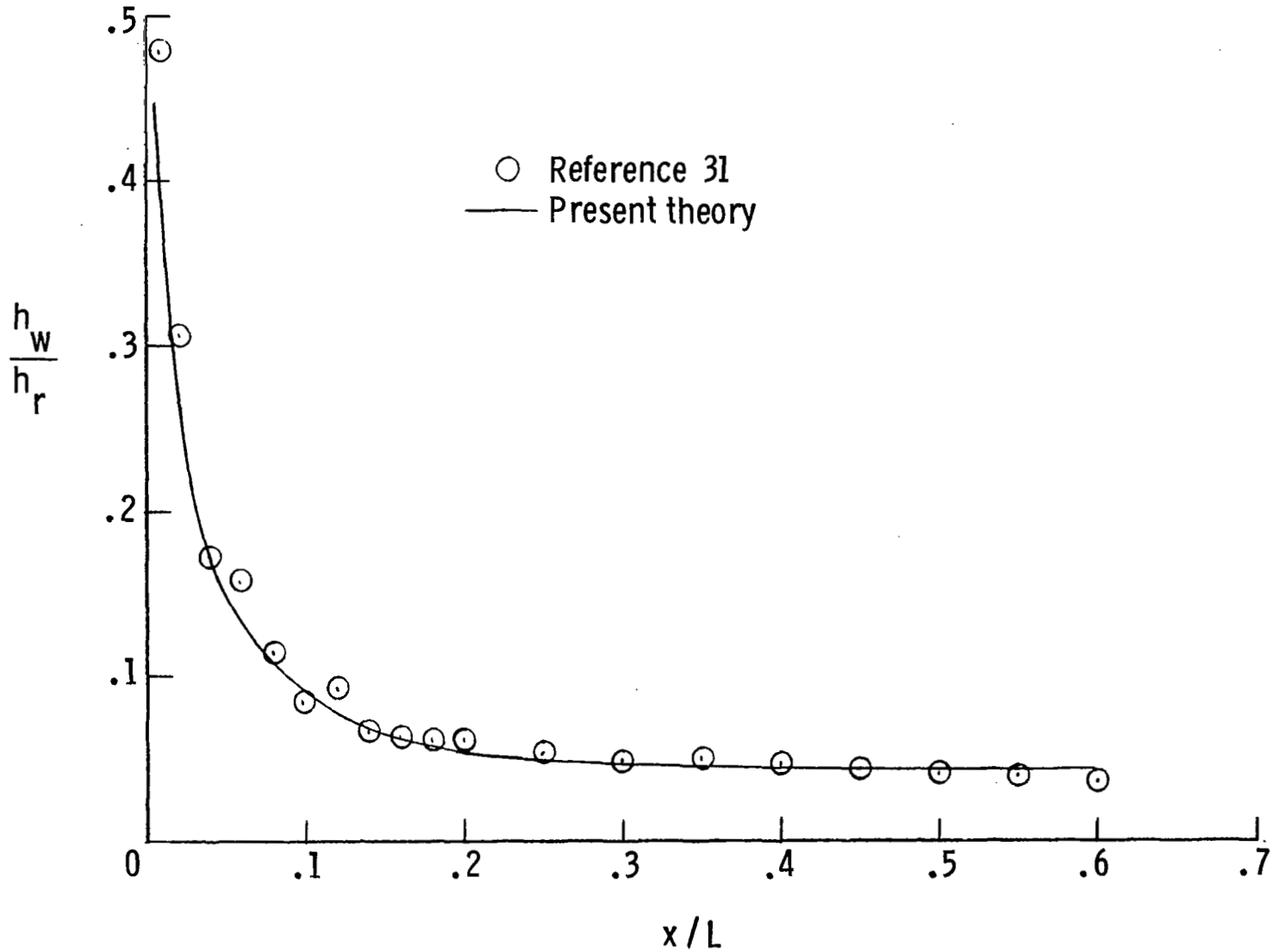
Figure 28.- Space Shuttle Orbiter type configuration.
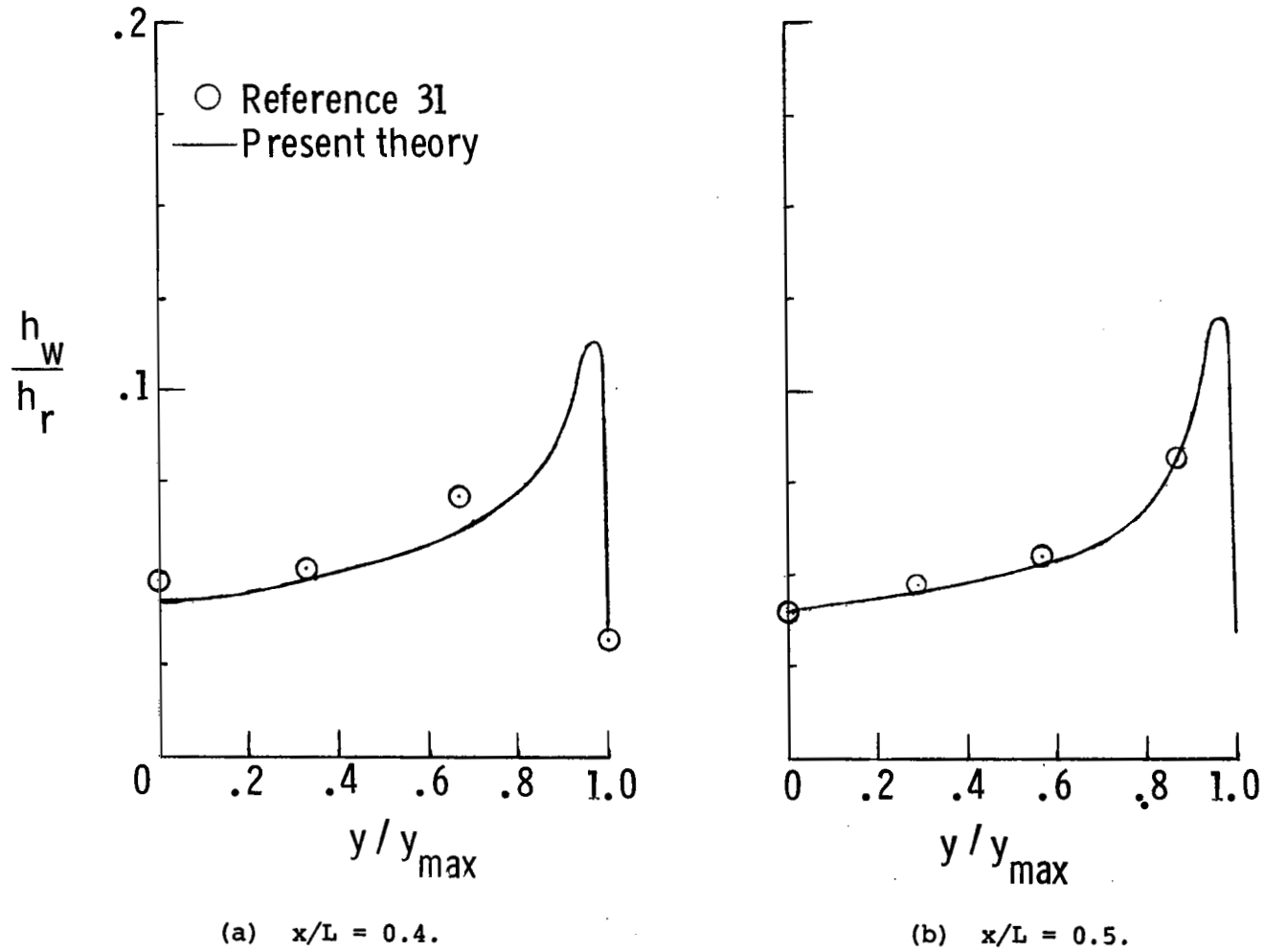
Figure 29.- Axial distribution of heat-transfer coefficient on Shuttle Orbiter type configuration at $\alpha = 20^\circ$. $M_\infty = 7.9$; $\gamma = 1.4$; $N_{Re,\infty} = 1.64 \times 10^6$ per meter; $\zeta_w = 0.31$; $h_r = 0.4984$ kW/m^2-s-K.

(a)   x/L = 0.4.

(b)   x/L = 0.5.

Figure 30.- Lateral distribution of heat-transfer coefficient
on Space Shuttle Orbiter type configuration at α = 20°.
M_∞ = 7.9; γ = 1.4; $N_{Re,\infty}$ = 1.64 × 10^6 per meter;
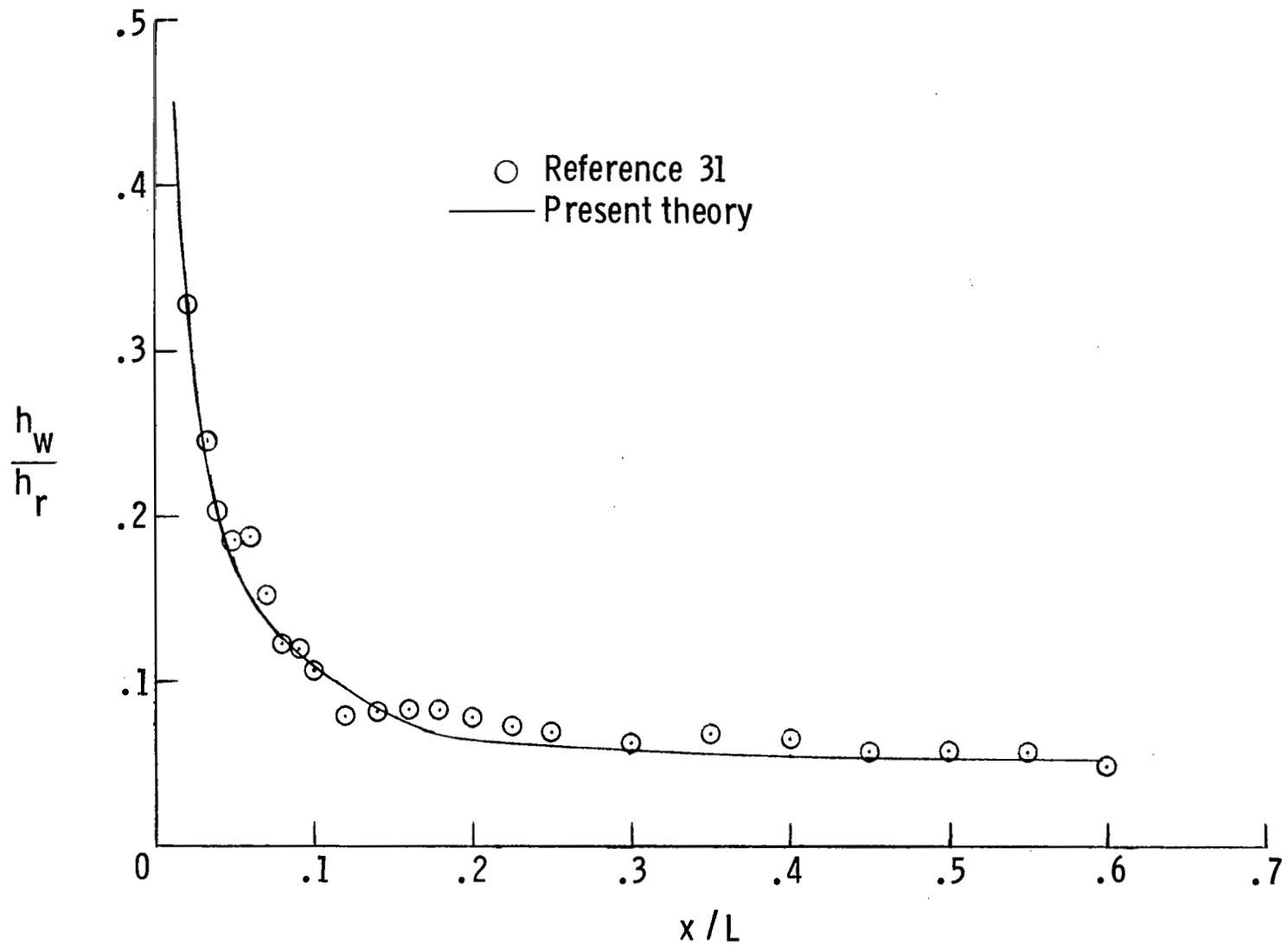ζ_w = 0.31; h_r = 0.4984 kW/m²-s-K.

Figure 31.- Axial distribution of heat-transfer coefficient on Space Shuttle Orbiter type configuration at $\alpha = 25^\circ$. $M_\infty = 7.9$; $\gamma = 1.4$; $N_{Re,\infty} = 1.64 \times 10^6$ per meter; $\zeta_w = 0.31$; $h_r = 0.4984$ kW/m^2-s-K.

1. Report No. NASA TP-1698	2. Government Accession No.	3. Recipient's Catalog No.
4. Title and Subtitle CALCULATION OF LAMINAR HEATING RATES ON THREE-DIMENSIONAL CONFIGURATIONS USING THE AXISYMMETRIC ANALOGUE		5. Report Date September 1980
		6. Performing Organization Code
7. Author(s) H. Harris Hamilton II		8. Performing Organization Report No. L-13748
		10. Work Unit No. 506-51-13-01
9. Performing Organization Name and Address NASA Langley Research Center Hampton, VA 23665		
		11. Contract or Grant No.
		13. Type of Report and Period Covered Technical Paper
12. Sponsoring Agency Name and Address National Aeronautics and Space Administration Washington, DC 20546		
		14. Sponsoring Agency Code

16. Abstract

A theoretical method has been developed for computing approximate laminar heating rates on three-dimensional configurations at angle of attack. The method is based on the axisymmetric analogue which is used to reduce the three-dimensional boundary-layer equations along surface streamlines to an equivalent axisymmetric form by using the metric coefficient which describes streamline divergence (or convergence). The method has been coupled with a three-dimensional inviscid flow field program for computing surface streamline paths, metric coefficients, and boundary-layer edge conditions.

17. Key Words (Suggested by Author(s)) Axisymmetric analogue Three-dimensional heating Boundary-layer flow	18. Distribution Statement Unclassified – Unlimited Subject Category 34
19. Security Classif. (of this report) Unclassified	20. Security Classif. (of this page) Unclassified	21. No. of Pages 77	22. Price A05

10   1 1U, D,   090380 S00903DS
DEPT OF THE AIR FORCE
AF WEAPONS LABORATORY
ATTN: TECHNICAL LIBRARY (SUL)
KIRTLAND AFB NM 87117

NASA